

Solving Nonlinear Parabolic Equations by a Strongly Implicit Finite-Difference Scheme

Applications to the Finite-Speed Spreading of Non-Newtonian Viscous Gravity Currents

Aditya A. Ghodgaonkar and Ivan C. Christov

Abstract We discuss the numerical solution of nonlinear parabolic partial differential equations, exhibiting finite-speed of propagation, via a strongly implicit finite-difference scheme with formal truncation error $\mathcal{O}[(\Delta x)^2 + (\Delta t)^2]$. Our application of interest is the spreading of viscous gravity currents in the study of which these type of differential equations arise. Viscous gravity currents are low Reynolds number (viscous forces dominate inertial forces) flow phenomena in which a dense, viscous fluid displaces a lighter (usually immiscible) fluid. The fluids may be confined by the sidewalls of a channel or propagate in an unconfined two-dimensional (or axisymmetric three-dimensional) geometry. Under the lubrication approximation, the mathematical description of the spreading of these fluids reduces to solving the so-called thin-film equation for the current's shape $h(x, t)$. To solve such nonlinear parabolic equations we propose a finite-difference scheme based on the Crank–Nicolson idea. We implement the scheme for problems involving a single spatial dimension (i.e., two-dimensional, axisymmetric or spherically-symmetric three-dimensional currents) on a uniform but staggered grid. We benchmark the scheme against analytical solutions and highlight its strong numerical stability by specifically considering the spreading of non-Newtonian power-law fluids in a variable-width confined channel-like geometry (a “Hele-Shaw cell”) subject to a given mass conservation/balance constraint. We show that this constraint can be implemented by re-expressing it as nonlinear flux boundary conditions on the domain's endpoints. Then, we show numerically that the scheme achieves its full second-order accuracy in space and time. Furthermore, we also highlight through numerical simulations how the proposed scheme respects, with high accuracy, the mass conservation/balance constraint.

Aditya A. Ghodgaonkar

School of Mechanical Engineering, Purdue University, West Lafayette, Indiana 47907, USA

Ivan C. Christov (✉)

School of Mechanical Engineering, Purdue University, West Lafayette, Indiana 47907, USA

e-mail christov@purdue.edu

1 Introduction

In his lucid 2015 book *Questions About Elastic Waves* [1], Engelbrecht asks “What is a wave?” and answers “As surprising as it may sound, there is no simple answer to this question.” Indeed, the definition of ‘wave’ depends on the physical context at hand [2]. Although most wave phenomena in classical continuum mechanics relate to a hyperbolic (wave) equation, one of the surprises of 20th century research into nonlinear partial differential equations (PDEs) is that *certain* parabolic (diffusion) equations also yield structures with finite speed of propagation. Two examples are (i) a linear diffusion equation with a nonlinear reaction term [3, 4], and (ii) a diffusion equations that is nonlinear due to a concentration-dependent diffusivity [5].¹ Indeed, it is known that certain aspects of wave phenomena can be reduced to a problem of solving a parabolic PDE, as gracefully illustrated by Engelbrecht [7, Ch. 6] through a series of selected case studies; further examples include, but are not limited to: electromagnetic waves along the earth’s surface [8], seismic waves [9], underwater acoustics [10], and the classical theory of nerve pulses [7, Sec. 6.4.2], which nowadays has been updated by Engelbrecht et al. [11] to a nonlinear hyperbolic (wave) model in the spirit of the Boussinesq paradigm [12, 13].

Of special interest to the present discussion are physical problems that are modeled by nonlinear parabolic PDEs. These nonlinear problems lack general, all-encompassing solution methodologies. Instead, finding a solution often involves methods that are specific to the nature of the governing equation or the physical problem it describes [14, Ch. 4] (see also the discussion in [2] in the context of heat conduction). The classical examples of nonlinear parabolic PDEs admitting traveling wave solutions come from heat conduction [15, Ch. X] (see also [16]) and thermoelasticity [16, 17]. The sense in which these nonlinear parabolic PDEs admit traveling-wave and ‘wavefront’ solutions now rests upon solid mathematical foundations [18, 19].

Another classical example of a nonlinear parabolic PDE governing the finite-speed wave-like motion of a substance arises in the study of an ideal gas spreading in a uniform porous medium [5]. A similar nonlinear parabolic equation was derived for the interface between a viscous fluid spreading horizontally underneath another fluid of lower density ($\Delta\rho > 0$ between the fluids) [20]. The motion of the denser fluid is dictated by a balance of buoyancy and viscous forces at a low Reynolds number (viscous forces dominate inertial forces). Such viscous gravity current flows are characterized by ‘slender’ fluid profiles i.e., they have small aspect ratios ($h/L \ll 1$, where h and L are typical vertical and horizontal length scales). Therefore, these flows can be modeled by lubrication theory [21, Ch. 6]. Generically, one obtains a nonlinear parabolic equation for the gravity current’s shape h as a function of the flow-wise coordinate x and time t . The case of the spreading of a fixed mass of New-

¹ More specifically, Barenblatt [5] (see also [6, p. 13]) credits the observation of finite-speed of propagation in nonlinear diffusion equations to a difficult-to-find 1950 paper by Zeldovich and Kompaneets.

tonian fluid was originally explored contemporaneously by Didden and Maxworthy [22] and Huppert [20].

Being governed by a parabolic (irreversible) equation, the these currents ‘forget’ their initial conditions at intermediate times; this is Barenblatt’s concept of *intermediate asymptotics* [23, 24]. It follows that a *universal* current profile can be obtained by a self-similarity transformation of the current shape $h(x, t)$, which reduces the PDE in eq. (1) to an ordinary differential equation (ODE). Since the similarity variable can obtained by a scaling (dimensional) analysis, this kind of solution is known as self-similarity of the *first* kind [24, Ch. 3]. Specifically, the transformation is of the form $h(x, t) = t^\beta f(\zeta)$, where $\zeta = x/(\eta_N t^\delta)$ is the similarity variable, and $f(\zeta)$ is the universal shape function to be determined by solving an ODE. The exponents β and δ are obtained through scaling (dimensional analysis) of the original PDE, and η_N is a constant to ensure ζ is dimensionless. An example of how this self-similar transformation is performed is discussed in the Appendix.

First-kind self-similarity has been used to analyze the propagation of Newtonian viscous gravity current flows in a variety of physical scenarios. For example, gravity currents arise in geophysical applications associated with flows through porous rocks [25] such as in ground water extraction [26], during oil recovery [27], and during CO₂ sequestration [28]. In these examples, the current shape $h(x, t)$ represents an interface between two immiscible fluids in the limit of large Bond number (gravity dominates surface tension). There is now an extensive literature featuring a wealth of exact and approximate analytical self-similar solutions for gravity currents in porous media, e.g., [5, 29–38] among many others. Non-Newtonian gravity currents obeying a power-law rheology (in which the denser fluid’s viscosity depends upon a power of the shear rate) [39–44] have also been studied, yielding further analytical self-similar solutions in closed form. Specifically, the solution of Ciriello et al [44] will be used herein to verify the truncation error and accuracy of the proposed numerical method.

For a self-similar solution to exist, both the governing PDE and its boundary conditions (BCs) must properly transform into an ODE in ζ with suitable BCs. A number of studies have specifically shown that the volume of fluid within the domain can be transient, varying as a power-law in time $\mathcal{V}(t) \propto t^\alpha$ ($\alpha \geq 0$) and a self-similar solution still exists (see, e.g., [5, 31, 33, 38, 42, 43] and the references therein). However, the nonlinear ODE in ζ often cannot be integrated exactly in terms of known function, except for $\alpha = 0$. In §2.2 below, we discuss how a constraint of the form $\mathcal{V}(t) \propto t^\alpha$ can be implemented numerically through flux BCs at the computational domain’s ends.

With increasing complexity of the flow physics incorporated in the model, finding a self-similarity transformation may no longer be possibly simply by using scaling (dimensional) arguments in certain cases. Gratton and Minotti [45] classified a number of such examples, including the so-called ‘focusing’ flows involving fluid axisymmetrically flowing towards the origin on a flat planar surface. Further examples involving confined currents in channels with variable width, and/or gravity currents in porous media whose permeability and porosity are functions of x , were proposed by Zheng et al [38] (see, e.g., figure 1). Though a self-similar transfor-

mation cannot be obtained by scaling arguments in these cases, the gravity currents nevertheless do enter a self-similar regime. Now, however, the exponents β and δ in the transformation are unknown *a priori*. This situation represents a self-similarity of the *second* kind [24, Ch. 4]. The governing nonlinear parabolic PDE can be transformed to a nonlinear ODE, then a nonlinear eigenvalue problem must be solved for β and δ through a phase-plane analysis [45, 46]. Alternatively, experiments or numerical simulations are necessary to determine β and δ . For example, early numerical simulations were performed to this end by Diez et al [47]. However, a ‘pre-wetting film’ ahead of the current’s sharp wavefront ($x = x_f(t)$ where $h(x_f(t), t) = 0$) was required to avoid numerical instabilities. The scheme therein was also first-order accurate in time only. In this chapter, we propose a modern, high-order-accurate implicit numerical method for use in such problems.

Specifically, we develop and benchmark a strongly implicit and conservative numerical scheme for one-dimensional nonlinear parabolic PDEs arising in the study of gravity currents. We show how the proposed scheme can be used to simulate (with high accuracy and at low computational expense) the spreading of one-dimensional *non-Newtonian* viscous gravity currents in variable geometries (specifically, Hele-Shaw cells with widths varying as a power law in x). To this end, we build upon the work of Zheng et al [38], which introduced this type of finite-difference scheme for simulating the spreading of a finite mass of Newtonian fluid in a variable-width Hele-Shaw cell. Owing to its accuracy and stability, the finite-difference scheme from [38] has been recently applied by Alhashim and Koch [48] to study hydraulic fracturing of low-permeability rock.

This chapter is organized as follows. In §2, we briefly summarize existing models describing certain flows of viscous gravity currents. Then, we introduce a convenient general notation for such nonlinear parabolic PDEs. The derivation of the BCs for the PDE, from the mass conservation constraint, is discussed in §2.2. Then, we construct the nonlinear Crank–Nicolson scheme in §3.2 and discuss the discretized form of the nonlinear flux BCs in §3.4. In §3.1, we introduce the one-dimensional uniform, staggered grid upon which the finite-difference scheme is to be implemented. Continuing, in §4.1, the scheme’s accuracy is justified by comparing the numerical solution provided by the finite-difference scheme (up to a specified physical time) against an analytical solution obtained through a self-similar transformation of the PDE. Specifically, this approach involves three validation cases: (i) a symmetric (about $x = 0$) lump of fixed fluid mass spreading in two directions (convergence independent of BCs), (ii) a fixed fluid mass spreading away from the origin ($x = 0$) (no fluid injection BCs), and (iii) a variable fluid mass being injected at the origin spreading away from it (requires careful implementation of the full nonlinear BCs). In all three cases, the scheme is shown to be capable of accurately computing the gravity current shape and its spreading in time. In §4.2, we analyze the scheme’s conservation properties by verifying numerically that it respects the mass constraint $\mathcal{V}(t) \propto t^\alpha$. We consider two validation cases: (i) release of a fixed fluid mass ($\alpha = 0$), and (ii) fluid mass injection into the domain ($\alpha > 0$). In both cases, we specifically focus on the challenging case of a non-Newtonian (power-law) displacing fluid in a

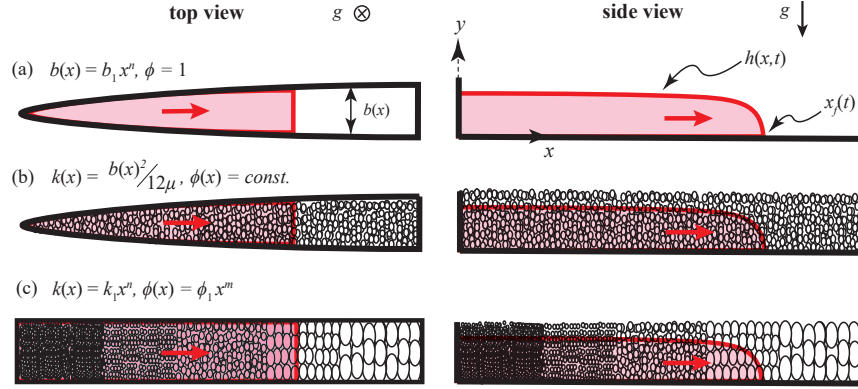


Fig. 1 A summary of the gravity current flows and domains considered in this work. (a) Flow away from the origin in a completely porous ($\phi = 1$) HS cell of variable width given by $b(x) = b_1 x^n$ ($b_1 = \text{const.}, 0 \leq n < 1$). (b) Flow in uniformly porous ($\phi = \phi_1 = \text{const.} \neq 1$) passage of variable width given by the same $b(x)$ as in (a). (c) Flow in a uniform-width slab (i.e., $b(x) = b_1 = \text{const.}$) with horizontally heterogeneous porosity and permeability given by $\phi(x) = \phi_1 x^m$ and $k(x) = k_1 x^n$ respectively. The effective permeability of the medium in (a) and (b) is set by the Hele-Shaw analogy via the width: $k(x) = [b(x)]^2/(12\mu)$. Figure reproduced and adapted with permission from [Zheng et al, Influence of heterogeneity on second-kind self-similar solutions for viscous gravity currents, J. Fluid Mech., vol. 747, p. 221] © Cambridge University Press 2014.

variable-width channel. As a benchmark, we use previously derived first-kind self-similar solutions from the literature, which are discussed in the Appendix.

2 Preliminaries

In this section, we summarize the mathematical model for viscous gravity currents in a selected set of applications involving Newtonian and non-Newtonian fluids. We study their spreading in a fixed- or variable-width channel geometry (a “Hele-Shaw cell”), as well as flows in heterogeneous porous media with independently variable permeability and porosity. Our goal is to highlight the fact that all these models can be concisely summarized by a single nonlinear parabolic PDE supplemented with a set of nonlinear Neumann (flux) BCs.

2.1 Fluid Domain and Flow Characteristics

The flow domain is assumed to be long and thin. For example, it can be a channel existing in the gap between two impermeable plates, i.e., a Hele-Shaw (HS) cell,

which may or may not have variable transverse (to the flow) width as shown in figure 1(a); or it can be slab of uniform-thickness heterogeneously porous material, as shown in figure 1(c). The viscous gravity current consists of one fluid displacing another immiscible fluid. Therefore, a sharp interface $y = h(x, t)$ separates the two fluids at all times. We consider the limit of negligible surface tension (i.e., negligible surface forces); as mentioned above this is the limit of large Bond number, $Bo \gg 1$. The density difference $\Delta\rho$ between the two fluids is considered large compared to the density of the lighter fluid, and the denser fluid flows along the bottom of the cell which is a horizontal, impermeable surface. In doing so, the denser fluid displaces the lighter fluid out of its way. Here, the geometry is considered to be vertically unconfined so that the flow of the upper, lighter fluid is negligible.

We are interested in the evolution of the interface $h(x, t)$ between the two fluids. Owing to the vertically unconfined, long and thin geometry of the flow passage, the denser fluid has a slender profile (low aspect ratio) and the fluid flow can be described by *lubrication theory*. The lubrication approximation also requires that the Reynolds number is small, $Re \ll 1$, which means that viscous forces dominate inertial forces in the flow. Therefore, in this limit of $Bo \gg 1$ and $Re \ll 1$, the flow is governed by a balance of viscous forces and gravity. Furthermore, the lubrication approximation allows us to neglect (at the leading order in the aspect ratio) the variation of quantities across the transverse direction, as well as the vertical velocities of the fluids.

As shown in figure 1(a), for the flow in a HS cell, we allow the cell's width to vary as a power-law of the streamwise coordinate x , i.e., $b(x) = b_1 x^n$, where $b_1 > 0$ is a dimensional constant, and $n \geq 0$ is a dimensionless exponent. Non-unity porosity can also be modelled by filling the HS cell with beads of fixed diameter as illustrated in figure 1(a). Since the cell has a variable width, it originates from a cell ‘origin,’ which is always taken to be $x = 0$ such that $b(0) = 0$. As discussed in [38], in such a flow geometry, the lubrication approximation may fail when $b(x)$ is an increasing function of x i.e., $db/dx = nb_1 x^{n-1} > 1$. In such quickly-widening cells, the transverse variations of properties become significant. We ensure the validity of the lubrication approximation, and models derived on the basis of it, by only considering $n < 1$ such that $b(x)$ remains a decreasing function of x .

As shown in figure 1(c), we also consider a gravity current spreading horizontally in a porous slab of constant transverse width ($b(x) = b_1 = \text{const.}$) with heterogeneous porosity $\phi(x) = \phi_1 x^m$ and permeability $k(x) = k_1 x^n$, which vary in the streamwise coordinate (see, e.g., [38]). Here, $m, n \geq 0$ are dimensionless exponents and $\phi_1, k_1 > 0$ are dimensional constants representing the porosity and permeability per unit width, respectively, in the case of constant-width slab with no streamwise variation ($m = n = 0$). These variations are illustrated by the streamwise changes of bead radii in figure 1(c). Now, the point at which the porosity and permeability vanish is the origin of the cell. Another interesting case, that of a medium with vertically heterogeneous porosity, has been explored by Ciriello et al [44]. In this chapter, we limit our discussion to flow in a completely porous (i.e., unobstructed, $\phi = 1$) HS cell of variable width as in figure 1(a). However, the numerical scheme

developed herein can readily treat any of these cases, taking the appropriate parameter definitions from table 1, as discussed in §2.2.

We allow the denser fluid to be non-Newtonian fluid. Specifically, it is assumed to obey the power-law rheology; this is also known as the Oswald–de Weale fluid [49]. In unidirectional flow, the shear stress is given by $\tau = \mu(\dot{\gamma})\dot{\gamma}$, where the dynamic viscosity μ depends on the shear rate $\dot{\gamma}$ as $\mu(\dot{\gamma}) = \mu_0\dot{\gamma}^{r-1}$. Here, μ_0 is the flow consistency index, and $r (> 0)$ is the fluid rheological index. Fluids having $r < 1$ are termed shear-thinning (e.g., blood), and fluids with $r > 1$ are termed shear-thickening (e.g., dense particulate suspensions). In the special case of $r = 1$, the power-law model reduces to the Newtonian fluid. As stated above, the nature of the displaced fluid is immaterial to the dynamics of the viscous gravity current, as long as the viscosity and density contrast is large. This condition is satisfied, for example, by assuming (for the purposes of this chapter) that air is the displaced fluid.

Finally, the volume of the fluid in the cell itself may be either fixed (constant mass) or vary with time (injection). Consistent with the literature, we consider the instantaneous volume of fluid in the cell to increase as a power law in t : $\mathcal{V}(t) = \mathcal{V}_{\text{in}}t^{\alpha}$, where $\alpha \geq 0$. In §2.2, we discuss how this assumption leads to BCs for the physical problem and for the numerical scheme.

2.2 Governing Equation, Initial and Boundary Conditions

The propagation of a viscous gravity current is described by a diffusion equation for the interface $h(x, t)$ between the fluids, which is also the shape of profile of the denser fluid. The models are derived either from porous medium flow under Darcy's law and the Dupoit approximation [26, Ch. 8] or using lubrication theory with no-slip along the bottom of the cell and zero shear stress at the fluid–fluid interface [21, Ch. 6-C]. The resulting velocity field is combined with a depth-averaged form of the continuity equation to derive the nonlinear parabolic PDE for $h(x, t)$. We propose to summarize all gravity current propagation along horizontal surfaces through a single 'thin-film' [50] equation:

$$\frac{\partial h}{\partial t} = \frac{A}{x^p} \frac{\partial}{\partial x} \left(x^q \psi \frac{\partial h}{\partial x} \right). \quad (1)$$

According to Engelbrecht [1, Ch. 5], eq. (1) can be classified as an 'evolution equation.' The term in the parentheses on the right-hand side of eq. (1), roughly, represents a fluid flux balanced by the change in height on the left-hand side. The multiplicative factor A/x^p arises due to (i) geometric variations of the flow passage in the flow-wise direction, (ii) porosity variations in the flow-wise direction, or (iii) from the choice of coordinate system in the absence of (i) or (ii). Here, A is dimensional constant depending on the flow geometry and domain, and fluid characteristics. Additionally, p and q are dimensionless exponents that depend on the flow geometry and fluid rheology. The quantity denoted by ψ represents specifically the *nonlinear*

ity in these PDEs, thus it is necessarily a function of h , and possibly $\partial h/\partial x$ for a non-Newtonian fluid (as in the third and fifth rows of table 1).²

As stated in §1, several versions of eq. (1) will be explored herein, incorporating geometric variations, porosity variations, non-Newtonian behavior. The pertinent physical scenarios that will be tackled by us using the numerical scheme developed herein are presented in table 1, which lists expressions for A , p , q and ψ .

The PDE (1) is solved on the finite space-time interval $(x, t) \in [\ell, L] \times [t_0, t_f]$. Here, t_0 and t_f represent the initial and final times of the numerical simulation's run, respectively. An initial condition (IC) $h_0(x)$ is specified at $t = t_0$, so that $h(x, t_0) = h_0(x)$ is known. Meanwhile, ℓ is small positive value (close to 0). Boundary conditions (BCs) are specified at $x = \ell$ and $x = L$. These involve some combination of h and $\partial h/\partial x$. The reason for taking $x = \ell \neq 0$ become clear when deriving these BCs.

Thus, let us now discuss such a suitable set of BCs. The BCs are based on the imposed mass conservation/growth constraint. Consider the case of a viscous gravity current in a porous slab with variable porosity $\phi(x) = \phi_1 x^m$ and transverse width $b_1 = \text{const.}$, which can either be set to unity or absorbed into ϕ_1 . Then, the conservation of mass constraint (see [38]) takes the form

$$\int_{\ell}^L h(x, t) \phi(x) dx = \mathcal{V}_{\text{in}} t^{\alpha}, \quad (2)$$

where $\alpha \geq 0$. In the parallel case of a HS cell with variable width $b(x) = b_1 x^n$ and porosity $\phi_1 = \text{const.}$, which can either be set to 1 or absorbed into b_1 , the mass constraint becomes

$$\int_{\ell}^L h(x, t) b(x) dx = \mathcal{V}_{\text{in}} t^{\alpha}. \quad (3)$$

Taking a time derivative of eq. (3) and employing eq. (1), we obtain

$$\begin{aligned} \frac{\partial}{\partial t} \int_{\ell}^L h(x, t) b_1 x^n dx &= \int_{\ell}^L \frac{\partial h}{\partial t} b_1 x^n dx = \int_{\ell}^L b_1 x^n \frac{A}{x^n} \frac{\partial}{\partial x} \left(x^q \psi \frac{\partial h}{\partial x} \right) dx \\ &= A b_1 \left(x^q \psi \frac{\partial h}{\partial x} \right) \bigg|_{x=\ell}^{x=L} \stackrel{\text{by (3)}}{=} \frac{d(\mathcal{V}_{\text{in}} t^{\alpha})}{dt} = \alpha \mathcal{V}_{\text{in}} t^{\alpha-1}. \end{aligned} \quad (4)$$

Here, $p = n$ in this case of interest, as described in table 1, and $A b_1 = \text{const.}$ Thus, we have obtained conditions relating $x^q \psi \partial h / \partial x$ at $x = \ell$ and $x = L$ to $\alpha \mathcal{V}_{\text{in}} t^{\alpha-1}$. These conditions, if satisfied, automatically take into account the imposed volume constraint from eq. (3). The calculation starting with eq. (2) is omitted as it is identical, subject to proper choice of p .

For the case of propagation away from the cell's origin (i.e., any injection of mass must occur near $x = 0$, specifically at $x = \ell$), to satisfy eq. (4), we can require that

² Interestingly, an 'r-Laplacian' PDE similar to eq. (1) for a power-law fluid in a HS cell (third row of table 1) arises during fluid-structure interaction between a power-law fluid and an enclosing slender elastic tube [51]. This PDE can also be tackled by the proposed finite-difference scheme.

$$\left(x^q \psi \frac{\partial h}{\partial x} \right) \Big|_{x=\ell} = \begin{cases} -\frac{\alpha B}{A} t^{\alpha-1}, & \alpha \neq 0, \\ 0, & \alpha = 0, \end{cases} \quad (5a)$$

$$\left(\psi \frac{\partial h}{\partial x} \right) \Big|_{x=L} = 0 \quad \Leftarrow \quad \frac{\partial h}{\partial x} \Big|_{x=L} = 0, \quad (5b)$$

where $B = \mathcal{V}_{\text{in}}/b_1$. The case of $\alpha > 0$ represents mass injection into the system. Although eq. (3) and eqs. (5) are equivalent, the imposition of the nonlinear BC in eqs. (5a) must be approached with care. It should be clear that to impose a flux near the origin (at $x = 0$), we need $(x^q \psi \partial h / \partial x) \Big|_{x \rightarrow 0}$ to be finite. Then, $\psi \partial h / \partial x = \mathcal{O}(1/x^q)$ as $x \rightarrow 0$. On the spatial domain $x \in (0, L)$, such an asymptotic behavior is possible for $p = q = 0$. However, for cases in a variable width cell ($p, q \neq 0$), the local profile and slope as $x \rightarrow 0$ blow up if they are to satisfy $\psi \partial h / \partial x = \mathcal{O}(1/x^q)$ as $x \rightarrow 0$. To avoid this uncomputable singularity issue, we defined the computational domain to be $x \in (\ell, L)$, where ℓ is ‘small’ but > 0 . The BC from eq. (5a) at $x = \ell$ can then be re-written as

$$\left(\psi \frac{\partial h}{\partial x} \right) \Big|_{x=\ell} = -\frac{\alpha B}{A \ell^q} t^{\alpha-1}, \quad \alpha > 0. \quad (6)$$

It may also be of interest to consider the case of a gravity current released a finite distance away from the origin and then spreading towards the origin. In this case, an additional length scale arises in the problem: the initial distance of the current’s edge from the origin, say $x_f(0)$. The existence of this extra length scale complicates the self-similarity analysis, leading to solutions of the second-kind [24, Ch. 4], as discussed in §1. However, the numerical scheme can handle this case without significant problem; in fact, it requires no special consideration, unlike spreading away from the origin. Now, we may simply take $\ell = 0$ and consider spreading on the domain $(0, L)$ subject to the following BCs:

$$\left(x^q \psi \frac{\partial h}{\partial x} \right) \Big|_{x \rightarrow 0} = 0 \quad \Leftarrow \quad \frac{\partial h}{\partial x} \Big|_{x=0} = 0, \quad (7a)$$

$$\left(\psi \frac{\partial h}{\partial x} \right) \Big|_{x=L} = \begin{cases} \frac{\alpha B}{A L^q} t^{\alpha-1}, & \alpha \neq 0, \\ 0, & \alpha = 0, \end{cases} \quad (7b)$$

which together allow us to satisfy eq. (4) and, thus, eq. (3).

The most significant advantage of defining nonlinear flux BCs, such as those in eqs. (5) or (7), is that a nonlinear nonlocal (integral) constraint, such as that in eq. (2) or (3), no longer has to be applied onto the solution $h(x, t)$. Furthermore, if we start with compact initial conditions, i.e., there exists a nose location $x = x_f(t_0)$ such that $h(x_f(t_0), t_0) = 0$, then the finite-speed of propagation property of the nonlinear PDE (1) [18, 19] ensures that this nose $x_f(t)$ exists for all $t > t_0$ and $h(x_f(t), t) = 0$ as well. The proposed fully-implicit scheme allows us to naturally capture this feature of the PDE, without any numerical instability, therefore we always solve the PDE on

the *fixed* domain $x \in (\ell, L)$ instead of attempting to rescale to a moving domain on which $x_f(t)$ is one of the endpoints. The latter approach proposed by Bonnecaze et al [52] (and used in more recent works [53] as well) leads to a number of additional variable-coefficient terms arising in the PDE (1), due to the non-Galilean transformation onto a shrinking/expanding domain. From a numerical methods point of view, having to discretize these additional terms is not generally desirable.

Having defined a suitable set of BCs, the last remaining piece of information required to close the statement of the mathematical problem at hand is the selection of a pertinent IC. For the case of the release of a finite fluid mass ($\alpha = 0$), an arbitrary polynomial initial condition may be selected, as long as it has zero slope at the origin ($x = 0$), leading to satisfaction of the no-flux boundary condition (5a). To this end, let the IC be given by

$$h_0(x) = \begin{cases} \frac{3C_0}{2} (x_0^\gamma - x^\gamma), & x \leq x_0, \\ 0, & x > x_0, \end{cases} \quad (8)$$

where x_0 is a ‘release-gate’ location defining the initial position of the current’s nose, i.e., $x_0 = x_f(t_0)$ and $h(x_f(t_0), t_0) \equiv h_0(x_0) = 0$. The constant $\gamma > 1$ is an arbitrary exponent. Finally, C_0 is set by normalizing $h_0(x)$ such that the initial volume of fluid corresponds to the selected fluid volume, \mathcal{V}_{in} , via eq. (3).

The case of the release of a finite mass of fluid is particularly forgiving in how we set the IC, and its slope at $x = 0$. In fact, we could even take $\gamma = 1$ in eq. (8) and the scheme will provide an initial flux of fluid at $t = t_0^+$, with $(\partial h / \partial x)_{x=0}$ thereafter. On the other hand, the case of mass injection ($\alpha \neq 0$) governed by the nonlinear BC is not as forgiving. By virtue of the ‘point-source’ mass injection at $x = \ell$, the slope at the origin sharply rises from the moment of mass injection. This very sharp rise has a tendency to introduce unphysical oscillations in the current profile when starting from the IC in eq. (8). To avoid this, we must select a ‘better’ IC, which has a shape more similar to the diverging solution near $x = 0$. Having tested a few different options, we found that an exponential function works well:

$$h_0(x) = \begin{cases} -a + be^{cx}, & x \leq x_0, \\ 0, & x > x_0. \end{cases} \quad (9)$$

Here, a, b and c are positive constants, and $x_0 = \frac{1}{c} \ln \frac{a}{b}$ ensures that the IC has no negative values and a sharp front.

Finally, it should be noted that the IC from eq. (8) is not used in the convergence studies for finite initial mass (§4.1.1 and §4.1.2). Rather, the IC is taken to be the exact self-similar solution of Ciriello et al [44] for a power-law non-Newtonian fluid in a uniform-width ($n = 0$) HS cell (see also the Appendix). The reasoning behind this particular choice is further expounded upon in §4.1.

Table 1 Selected models of the propagation of viscous gravity currents herein simulated by a finite-difference scheme.

| Case | A | p | q | ψ |
|--|---|-----|---------------------------------|--|
| Newtonian fluid, fixed-width HS cell: $b(x) = b_1$. (see Huppert and Woods [29]) | $\frac{\Delta \rho g b_1^2}{12\mu}$ | 0 | 0 | h |
| Newtonian fluid, variable-width HS cell: $b(x) = b_1 x^n$. (see Zheng et al [38]) | $\frac{\Delta \rho g b_1^2}{12\mu}$ | n | $3n$ | h |
| Power-law fluid: $\mu = \mu_0 \dot{\gamma}^{r-1}$, variable-with HS cell: $b(x) = b_1 x^n$. (generalized from Di Federico et al [43]) | $\left(\frac{r}{2r+1}\right) \left(\frac{\Delta \rho g}{\mu_0}\right)^{1/r} \left(\frac{b_1}{2}\right)^{(r+1)/r}$ | n | $n \left(\frac{2r+1}{r}\right)$ | $h \left \frac{\partial h}{\partial x}\right ^{(1-r)/r}$ |
| Newtonian fluid, 2D porous medium, variable porosity: $\phi(x) = \phi_1 x^m$, variable permeability: $k(x) = k_1 x^n$. (see Zheng et al [38]) | $\frac{\Delta \rho g k_1}{\mu \phi_1}$ | m | n | h |
| Power-law fluid: $\mu = \mu_0 \dot{\gamma}^{r-1}$, 2D porous medium, variable porosity: $\phi(x) = \phi_1 x^m$, variable permeability: $k(x) = k_1 x^n$. [†] (see Ciriello et al [44]) | $\left(\frac{\psi_{\text{in}}}{\phi_1}\right)^{\lambda_1} \left\{ 2^{(3r+1)/2} \frac{r}{3r+1} \left(\frac{k_1^{r+1}}{\phi_1^2}\right)^{1/2r} \left(\frac{\Delta \rho g}{\mu_0}\right)^{1/r} \right\}^{\lambda_2}$ | m | $\frac{m(r-1)+n(r+1)}{2r}$ | $h \left \frac{\partial h}{\partial x}\right ^{(1-r)/r}$ |

[†] $\lambda_1 = -\frac{q-n}{2-\alpha}$ and $\lambda_2 = 1 + \frac{(q-n)(\alpha-1)}{2-\alpha}$, q is the exponent from the third column, and α is the exponent from the volume constraint: $\mathcal{V} = \mathcal{V}_{\text{in}} t^\alpha$.

3 The Numerical Scheme

The proposed numerical method is a one-dimensional finite-difference scheme using the Crank–Nicolson approach toward implicit time-stepping. Our presentation follows recent literature, specifically the construction in [38, Appendix B]. The proposed scheme’s truncation error is formally of second order in both space and time, and we expect the scheme to be unconditionally stable. Furthermore, the scheme is conservative in the sense that it maintains the imposed time-dependency of the fluid volume with high accuracy via a specific set of nonlinear BCs. This section is devoted to discussing all these topics one by one.

3.1 Notation: Grids, Time Steps, and Grid Functions

The PDE (1) is solved on an equispaced one-dimensional grid of $N + 1$ nodes with grid spacing $\Delta x = (L - \ell)/(N - 1)$. The solution values are kept on a staggered grid of cell-centers, which are offset by $\Delta x/2$ with respect to the equispaced grid points. As a result, there is a node lying a half-grid-spacing beyond each domain boundary. It follows that the location of the i^{th} grid point on the staggered grid is $x_i = \ell + (i - 1/2)\Delta x$, where $i = 0, 1, 2, \dots, N$. A representative grid with 12 nodes is shown in figure 2. The use of a staggered grid affords additional stability to the scheme and allows the numerical discretization of Neumann BCs to be second-order accurate by default, using only two cell-centered values (as the boundary now lies half-way between two grid points).

As stated in §2.2, the PDE (1) is solved over a time period $t \in (t_0, t_f]$, such that $t_f > t_0 \geq 0$, where both the initial time t_0 and the final time t_f of the simulation are user defined. The scheme thus performs M discrete time steps each of size $\Delta t = (t_f - t_0)/(M - 1)$. The n^{th} time step advances the solution to $t = t^n \equiv t_0 + n\Delta t$, where $n = 0, 1, \dots, M - 1$. Finally, we define the discrete analog (‘grid function’) to the continuous gravity current shape, which we actually solve for, by $h_i^n \approx h(x_i, t^n)$.

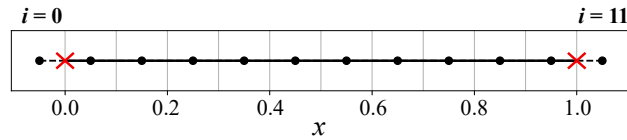


Fig. 2 A sample twelve-node equispaced, staggered, one-dimensional grid. The grid nodes are staggered by half a grid step $\Delta x/2$ from the cell faces. The actual domain boundaries are marked by X . Here, $\ell = 0$ and $L = 1$.

3.2 The Nonlinear Crank–Nicolson Scheme

Let us denote by \mathcal{L} the continuous spatial operator acting on h on the right-hand side of eq. (1), i.e.,

$$\mathcal{L}[h] \equiv \frac{A}{x^p} \frac{\partial}{\partial x} \left(x^q \psi \frac{\partial h}{\partial x} \right). \quad (10)$$

Since \mathcal{L} is a second-order spatial operator and, thus, eq. (1) is a diffusion equation, we are inclined to implement a second-order-accurate time-stepping by the Crank–Nicolson scheme [54]. The Crank–Nicolson scheme is fully implicit, which avoids the stringent restriction ($\Delta t \lesssim (\Delta x)^2$) suffered by explicit time discretizations of diffusion equations [55, Ch. 6]. Then, the time-discrete version of eq. (1) is

$$\frac{h_i^{n+1} - h_i^n}{\Delta t} = \frac{1}{2} (\mathcal{L}_d[h_i^{n+1}] + \mathcal{L}_d[h_i^n]), \quad (11)$$

where \mathcal{L}_d is the discrete analog to the continuous spatial operator \mathcal{L} defined in eq. (10). Based on the approach of Christov and Homsy [56], the discrete spatial operator is constructed via central differencing using two cell-face values, while staggering the nonlinear terms:

$$\mathcal{L}_d[h_i^n] = \frac{A}{x_i^p} \left[\frac{\left(x_{i+1/2}^q \psi_{i+1/2}^{n+1/2} \right) S_{i+1}^n - \left(x_{i-1/2}^q \psi_{i-1/2}^{n+1/2} \right) S_i^n}{\Delta x} \right], \quad (12a)$$

$$\mathcal{L}_d[h_i^{n+1}] = \frac{A}{x_i^p} \left[\frac{\left(x_{i+1/2}^q \psi_{i+1/2}^{n+1/2} \right) S_{i+1}^{n+1} - \left(x_{i-1/2}^q \psi_{i-1/2}^{n+1/2} \right) S_i^{n+1}}{\Delta x} \right], \quad (12b)$$

where $S \equiv \partial h / \partial x$ is the slope of the gravity current's shape. Note that the nonlinear terms, denoted by ψ , have been evaluated the same way, i.e., at the mid-time-step $n + 1/2$, for both $\mathcal{L}_d[h_i^n]$ and $\mathcal{L}_d[h_i^{n+1}]$.

Substituting eqs. (12) into eq. (11) results in a system of *nonlinear* algebraic equations because ψ is evaluated at mid-time-step $n + 1/2$ and, thus, depends on both h_i^n (known) and h_i^{n+1} (unknown). This system must be solved for the vector h_i^{n+1} ($i = 0, \dots, N$), i.e., the approximation to the gravity current's shape at the next time step. Solving a large set of nonlinear algebraic equations can be tedious and computationally expensive. A simple and robust approach to obtaining a solution of the nonlinear algebraic system is through fixed-point iterations, or ‘the method of internal iterations’ [57]. Specifically, we can iteratively compute approximations to h_i^{n+1} , the grid function at the new time step, by replacing it in eq. (11) with $h_i^{n,k+1}$, where $h_i^{n,0} \equiv h_i^n$. Then, the proposed numerical scheme takes the form:

$$\begin{aligned} \frac{h_i^{n,k+1} - h_i^n}{\Delta t} &= \frac{A}{2\Delta x} \left[\frac{x_{i+1/2}^q}{x_i^p} \psi_{i+1/2}^{n+1/2,k} S_{i+1}^{n,k+1} - \frac{x_{i-1/2}^q}{x_i^p} \psi_{i-1/2}^{n+1/2,k} S_i^{n,k+1} \right] \\ &+ \frac{A}{2\Delta x} \left[\frac{x_{i+1/2}^q}{x_i^p} \psi_{i+1/2}^{n+1/2,k} S_{i+1}^n - \frac{x_{i-1/2}^q}{x_i^p} \psi_{i-1/2}^{n+1/2,k} S_i^n \right]. \end{aligned} \quad (13)$$

The key idea in the method of internal iterations is to evaluate the nonlinear ψ terms at iteration k , while keeping the linear slopes S from the next time step $n+1$ at iteration $k+1$. This manipulation linearizes the algebraic system, at the cost of requiring iteration over k . Upon convergence of the internal iterations, h_i^{n+1} is simply the last iterate $h_i^{n,k+1}$. Before we can further discuss the iterations themselves or their convergence, we must define our discrete approximations for ψ and S .

The operator \mathcal{L}_d is essentially a second derivative, so we take inspiration from the standard way of constructing the three-point central finite-difference formula for the second derivative [55]. Specifically, it suffices to take the backward difference approximation with respect to the nearest grid point on the ‘right’ for the slopes S_i and S_{i+1} . For example, at any time step:

$$S_i \equiv \left(\frac{\partial h}{\partial x} \right)_{x=x_i} \approx \frac{h_i - h_{i-1}}{\Delta x}. \quad (14)$$

Next, following [38, 58], we evaluate ψ at $x_{i\pm 1/2}$ by averaging the known values at x_i and x_{i+1} or x_i and x_{i-1} , respectively. Likewise, to approximate $\psi^{n+1/2}$, we average the known values: ψ^n at t^n and $\psi^{n,k}$ at the previous internal iteration. In other words, our approximation of the nonlinear terms is

$$\psi_{i+1/2}^{n+1/2,k} = \frac{1}{2} \left[\underbrace{\frac{1}{2} (\psi_{i+1}^{n,k} + \psi_i^{n,k})}_{=\psi_{i+1/2}^{n,k}} + \underbrace{\frac{1}{2} (\psi_{i+1}^n + \psi_i^n)}_{=\psi_{i+1/2}^n} \right], \quad (15a)$$

$$\psi_{i-1/2}^{n+1/2,k} = \frac{1}{2} \left[\underbrace{\frac{1}{2} (\psi_i^{n,k} + \psi_{i-1}^{n,k})}_{=\psi_{i-1/2}^{n,k}} + \underbrace{\frac{1}{2} (\psi_i^n + \psi_{i-1}^n)}_{=\psi_{i-1/2}^n} \right]. \quad (15b)$$

Equations (15) afford improved stability for nonlinear PDEs, while preserving the conservative nature of the scheme (as will be shown in §4.2), as discussed by Von Rosenberg [59] who credits the idea of averaging nonlinear terms across time stages and staggered grid points to the seminal work of Douglas Jr. et al [60, 61].

Here, it is worthwhile noting that, while the classical Crank–Nicolson [54] scheme is *provably* unconditionally stable [55] when applied to a *linear* diffusion equation, it is suggested in [56] that the current approach provides additional stability to this nonlinear scheme even at large time steps. Since our problem is nonlinear, some care should be taken in evaluating how large of a time step could be taken. Nevertheless, it is still expected that the largest stable Δt will be independent of Δx .

A complication arising in the present context is that we focus on the case of a power-law non-Newtonian viscous gravity current spreading in a variable width cell. As a result, recalling table 1, this model features $\partial h/\partial x$ in ψ , *unlike* the Newtonian case. While the temporal accuracy of the scheme is ensured through the robust implementation of the nonlinear Crank–Nicolson time-stepping, the spatial accuracy is contingent upon the discretization of $\partial h/\partial x$ in ψ . A further consequence is that, once we discretize $\partial h/\partial x$, the discretization of ψ becomes *nonlocal* (i.e., it requires information beyond the i^{th} grid point). Nevertheless, the overall scheme still only requires a three-point stencil for \mathcal{L}_d . In particular, for interior grid points, we use a central-difference formula, giving rise to the expression (at any time step):

$$\psi_i \equiv \left[h \left| \frac{\partial h}{\partial x} \right|^{(1-r)/r} \right]_{x=x_i} \approx h_i \left| \frac{h_{i+1} - h_{i-1}}{2\Delta x} \right|^{(1-r)/r}. \quad (16)$$

This choice of approximation ensures second-order accuracy at all interior grid nodes. However, at the second ($i = 1$) and the penultimate ($i = N - 1$) nodes, the second-order accurate approximation to $\partial h/\partial x$ in $\psi_{i\pm 1/2}$ as defined in eqs. (15) requires the unknown values h_{-1} and h_{N+1} . To resolve this difficulty, we use ‘biased’ (backward or forward) three-point difference approximations:

$$\psi_0 \approx h_0 \left| \frac{-3h_0 + 4h_1 - h_2}{2\Delta x} \right|^{(1-r)/r}, \quad (17a)$$

$$\psi_N \approx h_N \left| \frac{3h_N - 4h_{N-1} + h_{N-2}}{2\Delta x} \right|^{(1-r)/r}. \quad (17b)$$

Finally, substituting the discretization for S from eq. (14) into eq. (13), it is possible to re-arrange the scheme into a tridiagonal matrix equation:

$$\begin{aligned} & \underbrace{\left[-\frac{A\Delta t}{2(\Delta x)^2} \frac{x_{i-1/2}^q}{x_i^p} \psi_{i-1/2}^{n+1/2,k} \right]}_{\text{matrix subdiagonal coefficient}} h_{i-1}^{n,k+1} \\ & + \underbrace{\left[1 + \frac{A\Delta t}{2(\Delta x)^2} \left(\frac{x_{i+1/2}^q}{x_i^p} \psi_{i+1/2}^{n+1/2,k} + \frac{x_{i-1/2}^q}{x_i^p} \psi_{i-1/2}^{n+1/2,k} \right) \right]}_{\text{matrix diagonal coefficient}} h_i^{n,k+1} \\ & + \underbrace{\left[-\frac{A\Delta t}{2(\Delta x)^2} \frac{x_{i+1/2}^q}{x_i^p} \psi_{i+1/2}^{n+1/2,k} \right]}_{\text{matrix superdiagonal coefficient}} h_{i+1}^{n,k+1} \\ & = h_i^n + \frac{A\Delta t}{2(\Delta x)^2} \left[\frac{x_{i+1/2}^q}{x_i^p} \psi_{i+1/2}^{n+1/2,k} (h_{i+1}^n - h_i^n) - \frac{x_{i-1/2}^q}{x_i^p} \psi_{i-1/2}^{n+1/2,k} (h_i^n - h_{i-1}^n) \right] \quad (18) \end{aligned}$$

for the interior grid points $i = 1, \dots, N - 1$. In eq. (18) the right-hand side and the variable coefficients in brackets on the left-hand side are both known, based on $h_i^{n,k}$, at any given internal iteration k . Then, each internal iteration involves the inversion of a tridiagonal matrix to solve for the grid function $h_i^{n,k+1}$. The inversion of this tridiagonal matrix can be performed efficiently with, e.g., ‘backslash’ in MATLAB. Subsequently, the coefficient matrix must be recalculated for each internal iteration because of the dependency of $\psi_{i\pm 1/2}^{n+1/2,k}$ on $h_i^{n,k}$ arising from eqs. (15) and (16).

The iterations in eq. (18) are initialized with $h_i^{n,0} = h_i^n$ ($i = 0, \dots, N$) and continue until an iteration $k + 1 = K$ is reached at which a 10^{-8} relative error tolerance is met. Specifically,

$$\max_{0 \leq i \leq N} |h_i^{n,K} - h_i^{n,K-1}| < 10^{-8} \max_{0 \leq i \leq N} |h_i^{n,K-1}|. \quad (19)$$

Typically only a small number (typically, less than a dozen) of internal iterations are required at each time step, making the scheme, overall, quite efficient.

A detail remains, however. The algebraic system defined in eq. (18) applies to all *interior* nodes, i.e., $i = 1, \dots, N - 1$. To complete the system, we must define rows $i = 0$ and $i = N$, which arise from the proper numerical approximation of the nonlinear BCs, which comes in §3.4. Upon completing the latter task successfully, $h_i^{n,K}$ becomes the grid function at the next time step h_i^{n+1} upon the completion of the internal iterations, and the time stepping proceeds.

3.3 The Special Case of Linear Diffusion

A special case of the proposed finite-difference scheme can be considered by setting the dimensionless exponents $p = q = 0$ (i.e., no spatial variation of the diffusivity) and $\psi = 1$ (linear diffusion). Accordingly, eq. (18) can be simplified and rearranged in the form ($i = 1, \dots, N - 1$):

$$\left[1 + \frac{A\Delta t}{(\Delta x)^2} \right] h_i^{n+1} = \frac{A\Delta t}{(\Delta x)^2} (h_{i-1}^{n+1} + h_{i+1}^{n+1} + h_{i-1}^n + h_{i+1}^n) + \left[1 + \frac{A\Delta t}{(\Delta x)^2} \right] h_i^n. \quad (20)$$

If the grid function $h_i^n \approx h(x_i, t^n)$ represents the temperature field along a one-dimensional rigid conductor situated on $x \in [\ell, L]$, eq. (20) is then the original second-order (in space and time) numerical scheme proposed by Crank and Nicolson [54] to solve a linear (thermal) diffusion equation [55, §6.3]. As such, this simplification helps illustrate the mathematical roots of the current scheme, and how we have generalized the classical work.

3.4 Implementation of the Nonlinear Boundary Conditions

As discussed in section 2.2, the boundary conditions are a manifestation of the global mass conservation constraint, eq. (2) or (3), imposed on eq. (1). The BCs described in eqs. (5) and (7) are defined at the ‘real’ boundaries of the domain, i.e., at $x = \ell$ and $x = L$. The numerical scheme implements these over the staggered grid. This allows for derivatives at $x = \ell$ and $x = L$ to be conveniently approximated using central difference formulas using two nearby staggered grid points. In this manner, the BC discretization maintains the scheme’s second order accuracy in space and time. Accordingly, for the case of a current spreading away from the cell’s origin, eqs. (5) are discretized in a ‘fully-implicit’ sense (to further endow numerical stability and accuracy to the scheme [58]) as follows:

$$\psi_{1/2}^{n+1/2,k} \frac{1}{\Delta x} (h_1^{n,k+1} - h_0^{n,k+1}) = \begin{cases} -\frac{\alpha B}{A\ell^q} t^{\alpha-1}, & \alpha \neq 0, \\ 0, & \alpha = 0, \end{cases} \quad (21)$$

$$\frac{1}{\Delta x} (h_N^{n,k+1} - h_{N-1}^{n,k+1}) = 0. \quad (22)$$

Within the internal iterations, however, $\psi_{1/2}^{n+1/2,k}$ is known independently of $h_1^{n,k+1}$ and $h_0^{n,k+1}$. Hence, we can express the first ($i = 0$) and last ($i = N$) rows in the tridiagonal matrix, whose interior rows are constructed from eq. (18), as

$$h_1^{n,k+1} - h_0^{n,k+1} = \begin{cases} -\frac{4\alpha B t^{\alpha-1} \Delta x}{A\ell^q (\psi_0^n + \psi_1^n + \psi_0^{n,k} + \psi_1^{n,k})}, & \alpha \neq 0, \\ 0, & \alpha = 0, \end{cases} \quad (23a)$$

$$h_N^{n,k+1} - h_{N-1}^{n,k+1} = 0. \quad (23b)$$

Similarly, we can derive the discretized BCs for spreading of a current towards the origin, when released a finite distance away from the origin, from eqs. (7). The, the first ($i = 0$) and last ($i = N$) rows in the tridiagonal matrix are expressed as

$$h_1^{n,k+1} - h_0^{n,k+1} = 0, \quad (24a)$$

$$h_N^{n,k+1} - h_{N-1}^{n,k+1} = \begin{cases} \frac{4\alpha B t^{\alpha-1} \Delta x}{A L^q (\psi_{N-1}^n + \psi_{N-2}^n + \psi_{N-1}^{n,k} + \psi_{N-2}^{n,k})}, & \alpha \neq 0, \\ 0, & \alpha = 0. \end{cases} \quad (24b)$$

4 Convergence and Conservation Properties of the Scheme

At this point, the numerical scheme and boundary conditions defined in eqs. (18) and (23) form a complete description of the numerical solution to the parabolic PDE from eq. (1), for a gravity current propagating away from the origin. We have claimed that the finite-difference scheme is conservative (i.e., it accurately maintains the imposed time-dependency of the fluid volume described in eq. (3)) and has second-order convergence. These aspects of the scheme will be substantiated in §4.1 and §4.2, respectively. For definiteness, we take the fluid properties to be $\Delta\rho = 1250.9 \text{ kg/m}^3$ and $\mu_0 = 0.6211 \text{ Pa}\cdot\text{s}^2$, which correspond to those of 95% glycerol-water mixture ($r = 1$) in air at 20°C (see [62, 63]). The computational domain's end is fixed at $L = 0.75 \text{ m}$ for all simulations.

4.1 Estimated Order of Convergence

First, we seek to justify the formal order of accuracy of the proposed scheme through carefully chosen numerical examples. To do so, we consider successively ‘more complicated’ cases from a numerical perspective. First, we simulate the case of a centrally released fixed mass of fluid propagating in two directions (§4.1.1). Second, we simulate the unidirectional spreading of a fixed mass of fluid (§4.1.2). Third, and last, we simulate the unidirectional spreading of a variable fluid mass (§4.1.3), i.e., we take into account injection of fluid at the boundary.

In each of these three cases, there is a need for a reliable benchmark solution against which the numerical solutions on successively refined spatial grids can be compared. For the case of the release of a fixed mass of fluid, an exact self-similar solution is provided by Ciriello et al [44]. Specifically the solution considers a power-law fluid in uniform HS cell ($n = 0$). The derivation of the self-similar solution is briefly discussed in the Appendix. We use this solution as the benchmark. As mentioned in §1, parabolic equations ‘forget’ their IC and the solution becomes self-similar after some time. However, for a general PDE, it is difficult (if not impossible) to estimate how long this process takes. Therefore, to ensure a proper benchmark against the exact self-similar solution, we start the simulation with the exact self-similar solution evaluated at some non-zero initial time ($t_0 > 0$). Using the latter as the initial condition, we allow the current to propagate up to a final time t_f , with the expectation that the current will thus remain in the self-similar regime for all $t \in (t_0, t_f]$. Comparing the final numerical profile with the exact self-similar solution at $t = t_f$ then allows for a proper benchmark.

To quantify the error between a numerical solution h_{num} and a benchmark h_{exact} solution at $t = t_f$, we use three standard function-space norms [14]:

$$\|h_{\text{num}}(x, t_f) - h_{\text{exact}}(x, t_f)\|_{L^\infty} = \max_{x \in [\ell, L]} |h_{\text{num}}(x, t_f) - h_{\text{exact}}(x, t_f)|, \quad (25\text{a})$$

$$\|h_{\text{num}}(x, t_f) - h_{\text{exact}}(x, t_f)\|_{L^1} = \int_\ell^L |h_{\text{num}}(x, t_f) - h_{\text{exact}}(x, t_f)| \, dx, \quad (25\text{b})$$

$$\|h_{\text{num}}(x, t_f) - h_{\text{exact}}(x, t_f)\|_{L^2} = \sqrt{\int_\ell^L |h_{\text{num}}(x, t_f) - h_{\text{exact}}(x, t_f)|^2 \, dx}. \quad (25\text{c})$$

Using a second-order trapezoidal rule for the integrals, the definitions in eqs. (25) can be expressed in terms of the grid functions to define the ‘errors’:

$$L_{\text{error}}^\infty \equiv \max_{0 \leq i \leq N} |h_i^M - h_{\text{exact}}(x_i, t_f)|, \quad (26\text{a})$$

$$L_{\text{error}}^1 \equiv \Delta x \left\{ \frac{1}{2} \left[|h_0^M - h_{\text{exact}}(x_0, t_f)| + |h_N^M - h_{\text{exact}}(x_N, t_f)| \right] + \sum_{i=1}^{N-1} |h_i^M - h_{\text{exact}}(x_i, t_f)| \right\}, \quad (26\text{b})$$

$$L_{\text{error}}^2 \equiv \left[\Delta x \left\{ \frac{1}{2} \left[|h_0^M - h_{\text{exact}}(x_0, t_f)|^2 + |h_N^M - h_{\text{exact}}(x_N, t_f)|^2 \right] + \sum_{i=1}^{N-1} |h_i^M - h_{\text{exact}}(x_i, t_f)|^2 \right\} \right]^{1/2}, \quad (26\text{c})$$

where M is the time step at which $t^M = t_f$.

Since the solution actually has a corner (derivative discontinuity) at the nose (wavefront) $x_f(t)$ such that $h(x_f(t), t) = 0$, then the propagating gravity current is in fact only a *weak* solution to the PDE [14]. Therefore, the L^∞ norm is not a good one to measure the error, as we do not expect the solution to ‘live’ in this function space. Nevertheless, our numerical results show convergence in the L^∞ norm. The natural functional space for solutions of eq. (1) is the space of integrable functions, i.e., L^1 . Indeed, we observe excellent second-order convergence in this norm. For completeness, the L^2 norm (commonly the function-space setting for parabolic equations [14, Ch. 7]) is considered as well. While we observe convergence close to second order in this norm as well, it is clearly not the ‘natural’ one for these problems either.

For our estimated-order-of-convergence study, Δx is successively halved on a domain of fixed length, such that on the c^{th} iteration of the refinement, the grid spacing is $\Delta x_c = \Delta x_0 / 2^{c-1}$, where Δx_0 is the initial grid spacing. Doing so ensures a set of common grid points (corresponding to the same physical locations) between successively refined grids. In all studies in this section, we begin with a grid with $N = 101$ nodes, and it becomes the coarsest grid for the refinement study. Given the (formally) unconditionally stable nature of the scheme, we take $\Delta t = 2\Delta x$ for the refinement studies without loss of generality. From a computational standpoint, it is desirable that time step and grid spacing are of the same order of magnitude in the estimated-order-of-convergence study.

4.1.1 Central Release of a Fixed Fluid Mass (No Boundary Effects)

Consider a symmetric domain $x \in [-L, +L]$. Then suppose that a fixed mass of fluid (i.e., $\alpha = 0$ in the volume constraint in eq. (3)) is released with an initial shape that is symmetric about $x = 0$. The final simulation time t_f is such that the gravity current does not reach $x = \pm L$ for $t \leq t_f$. Since the fluid mass is constant and the BCs are imposed at $x = \pm L$ (where $h = 0$ initially and remains so for all $t \leq t_f$, by construction), their discretization simply reduces to the simplest cases, i.e., eqs. (24a) and (23b). Thus, the BCs for this study are simply linear Neumann (no flux or homogeneous) BCs, and they do not influence the order of convergence of the overall scheme. Therefore, this study allows us to verify that our approach to the treatment of the nonlinearity ψ , and its weighted averages appearing in the spatially discretized operator \mathcal{L}_d in eq. (12), deliver the desired second-order accuracy in space. Coupled with the Crank–Nicolson time-stepping’s second-order accuracy in time, we thus expect the second order of convergence in this refinement study.

As stated above, we take the exact self-similar solution to eq. (1) provided by Ciriello et al [44] (and discussed in the Appendix) evaluated at $t = t_0$ and mirrored about $x = 0$ as the IC. Upon evolving this IC numerically up to $t = t_f$, we compare the numerical profile to the same exact solution now evaluated at $t = t_f$. Hence, in accordance with the assumptions required to obtain this exact solution in [44], we limit this first convergence study to a uniform-width HS cell, i.e., $n = 0$.

Figure 3 shows the propagation of constant-mass viscous gravity current of three different fluids: (a) Newtonian, (b) shear-thinning and (c) shear-thickening power-law. The currents propagate symmetrically about the center of the domain ($x = 0$). The sharp moving front $x_f(t)$ is accurately captured in these simulations on fairly modest (i.e., coarse) grids, without *any* signs of numerical instability or need for special treatment of the derivative discontinuity. Computing the error as a function of Δx during the grid refinement, shows second-order convergence. This numerical example thus indicates that the proposed approach to treating the implicit nonlinear ψ terms, specifically their evaluation at $n + 1/2$, is consistent with the desired second-order accuracy.

It should be noted that the restriction on t_f , necessary so that the current does not reach the domain boundaries, is critical since the chosen benchmark exact solution only describes the ‘spreading’ behavior of the current and not its ‘levelling’ (once it reaches the no-flux boundaries at $x = \pm L$). Indeed, the levelling regime possesses its distinct self-similar behavior (see, e.g., [47, 64]), which is beyond the scope of the present work.

4.1.2 Propagation of a Fixed Mass of Fluid in a Single Direction

To ascertain the accuracy of our discretization of the nonlinear BCs, we now return to a one-sided domain $x \in [\ell, L]$ with $\ell = 0$. For the case of the current spreading away from the origin, the BC at the ‘left’ end of the domain (from which the fluid is released) is non-trivial, and its proper discretization is key to the overall order

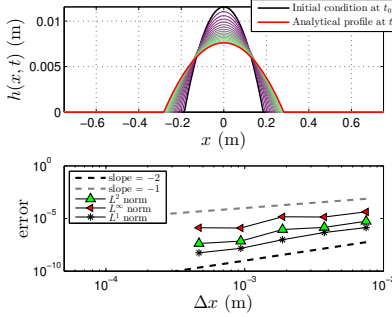
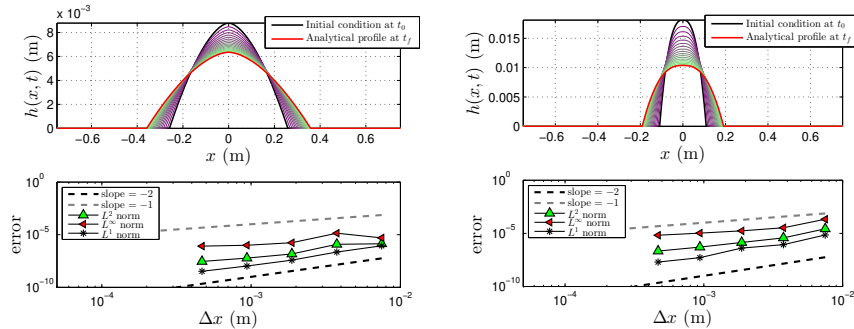
(a) Newtonian fluid ($r = 1$).(b) Shear-thinning fluid ($r = 0.7$).(c) Shear-thickening fluid ($r = 1.6$).

Fig. 3 Estimated order-of-convergence of a ‘centrally released’ fixed fluid mass propagating in both directions in a uniform-width HS cell ($n = 0$). The currents’ shapes are plotted from early times (purple/dark) to late times (green/light). In all cases, the volume of fluid is $\mathcal{V}_{\text{in}} = 2.4902 \times 10^{-5} \text{ m}^3$ and $b_1 = 0.01739 \text{ m}$. The currents are released at $t_0 = 1 \text{ s}$ and spread until $t_f = 3.5 \text{ s}$.

of the convergence of the scheme. Conveniently, for a fixed mass ($\alpha = 0$), the BCs still reduce to homogeneous Neumann conditions (recall §3.4), however, h is no longer zero at the boundary (as was the case in §4.1.1). Now, we benchmark this successively ‘more complicated’ case.

Once again we ensure that t_f is such that the current does not reach the downstream ($x = L$) domain end. Then, similar to §4.1.1, we can once again use the exact solution of Ciriello et al [44] as the benchmark exact solution; again, this requires restricting to uniform-width HS cells (i.e., $n = 0$).

Figure 4 shows clear second-order estimated rate-of-convergence in the L^1 norm. This result indicates the decision to implement the scheme on a staggered grid, in which case the Neumann BCs (for $\alpha = 0$) are conveniently discretized using two-point central differences at the boundary, was indeed the correct decision.

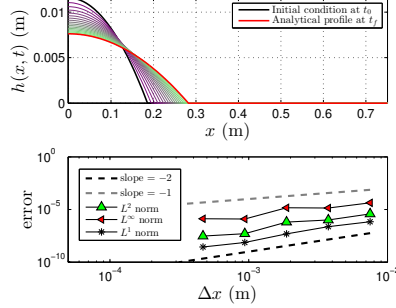
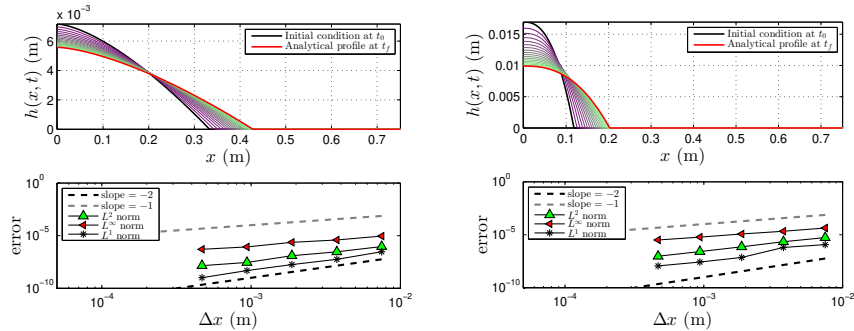
(a) Newtonian fluid ($r = 1$).(b) Shear-thinning fluid ($r = 0.5$).(c) Shear-thickening ($r = 1.5$).

Fig. 4 Estimated order-of-convergence study for the release of a fixed fluid mass propagating in a single direction (away from cell's origin) in a uniform-width HS cell ($n = 0$). Once again, the currents are released at $t_0 = 1$ s and spread until $t_f = 3.5$ s. The currents' shapes are plotted from early times (purple/dark) through late times (green/light). The remaining model parameters for these simulations are the same as in figure 3.

4.1.3 Propagation in a Single Direction with Mass Injection

Finally, we subject the numerical scheme to its most stringent test yet. That is, we compute the estimated order of convergence under mass injection conditions ($\alpha \neq 0$). The injection occurs near the cell's origin and the current propagates away from this location. Since $\alpha \neq 0$, the fully nonlinear forms of the BCs as given in eqs. (5) and (7) now come into play.

Unlike the previously discussed cases of the release of a fixed fluid mass, a straightforward exact solution to the nonlinear ODE emerging from the self-similar analysis is not possible. For a variable mass, obtaining a benchmark solution from the self-similar analysis is now significantly more challenging, given that the nonlinear ODE must be solved *numerically* (see the Appendix). Despite the availability of accurate stiff ODE solvers, such as `ode15s` in MATLAB, it is quite difficult to map the numerical solution of the self-similar ODE onto the selected computational grid,

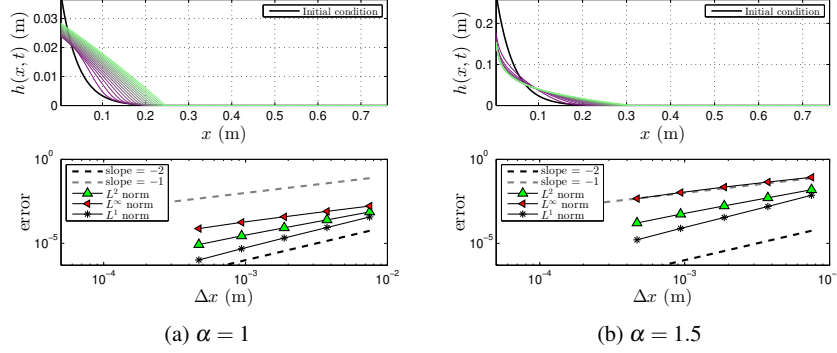


Fig. 5 Estimated order-of-convergence study for a variable-mass gravity current with injection at $x = \ell$ on the truncated domain $x \in [\ell, L]$ with $\ell = \Delta x_0$. Simulations are shown for the case of (a) a Newtonian fluid in a uniform-width HS cell ($r = 1, n = 0$), and (b) a shear-thickening fluid in a variable width cell ($r = 0.6, n = 0.6$). The remaining model parameters for these simulations are the same as in figure 3.

and maintain the desired order of accuracy throughout this procedure. Therefore, in this numerical study, we instead elect to use a ‘fine-grid’ numerical solution as the benchmark solution. This benchmark solution is then compared against the solutions on successively coarser grids to establish the estimated order of convergence of the numerical scheme.

For this study, the simulation domain is $x \in [\ell, L]$ with $\ell = \Delta x_0$, so that $x_{i=0} = \ell - \Delta x_0/2$ and $x_{i=N} = L + \Delta x_0/2$, and the boundary points are at the same cell faces on all grids during the refinement. The IC at $t_0 = 0$ s is the one given in eq. (9) with $a = 0.001$, $b = 0.35$, $c = 25$. The solution is advanced numerically up to $t_f = 1.5$ s.

Figure 5 shows that the order of convergence of the numerical method is second order in space and time in the L^1 norm, as expected. In this figure, to show some variety, we present two distinct but arbitrarily selected cases: (a) a Newtonian fluid in a uniform-width HS cell ($n = 0$) with volume growth exponent $\alpha = 1$, and (b) a non-Newtonian (shear-thinning, $r = 0.6$) fluid in a shaped HS cell (width exponent $n = 0.6$) with the volume growth exponent $\alpha = 1.5$. Second-order convergence is observed in both cases.

With this final numerical test, we have justified the formal truncation error of the proposed numerical scheme. This result is nontrivial because the PDE and the scheme are both *nonlinear*, requiring subtle approximation on a staggered grid, across half-time steps, and linearization of algebraic system via internal iterations.

4.2 Satisfaction of the Mass Constraint at the Discrete Level

Since the BCs derived in §2.2 (and discretized in §3.4) stem from the mass conservation constraint (i.e., eq. (2) or eq. (3)), it is expected that the proposed finite-difference scheme should produce a solution $h(x, t)$ that satisfies eq. (2) or eq. (3) to within $\mathcal{O}[(\Delta x)^2 + (\Delta t)^2]$ or better, if this constraint is checked independently again after computing the numerical solution. To verify this capability of the scheme, in this subsection, we consider two cases: (i) a fixed fluid mass released near the origin ($\alpha = 0$), and (ii) spreading subject to mass injection ($\alpha > 0$) near the origin. Both cases are studied on the domain $x \in [\ell, L]$ with $\ell = \Delta x$. The solution is evolved on the time interval $t \in (t_0, t_f]$, and the volume error for each t is computed as

$$\left| \int_{\ell}^L h(x, t) b_1 x^n dx - \mathcal{V}_{\text{in}} t^{\alpha} \right|, \quad (27)$$

where the x -integration is performed by the trapezoidal rule to $\mathcal{O}[(\Delta x)^2]$ on the staggered mesh, as before. We expect that the volume error, as defined in eq. (27), is $\mathcal{O}[(\Delta x)^2 + (\Delta t)^2]$, the same as the overall scheme. In this numerical study, the selection of the IC is no longer critical, as we do not compare against an exact self-similar solution. Accordingly, we select generic ICs from eqs. (8) and (9).

4.2.1 Fixed Mass Release ($\alpha = 0$)

In this case, the IC is a cubic polynomial determined from eq. (8) with $\gamma = 3$, $x_0 = 0.25$ m. The error in the total fluid volume as a function of t is compared with the initial one. Figure 6 shows that, while numerical error does build up in the total volume, the initial volume remain conserved to within (or better than) $(\Delta t)^2 = 10^{-6}$.

4.2.2 Mass Injection ($\alpha > 0$)

A more stringent test of conservation properties of the proposed scheme is conducted by applying the nonlinear BC associated with imposed mass injection at one end. For this case, the IC is taken to be the function in eq. (9) with $a = 0.001$ m, $b = 0.35$ m and $c = 25 \text{ m}^{-1}$ and $x_0 = \frac{1}{c} \ln \frac{a}{b}$. A combination of n , r and α values have been considered to highlight the conservation properties across different physical regimes. Figure 7 shows that, in all cases, the volume constraint is properly respected; while the volume error builds up, it remains small (within or better than $(\Delta t)^2 = 10^{-6}$).

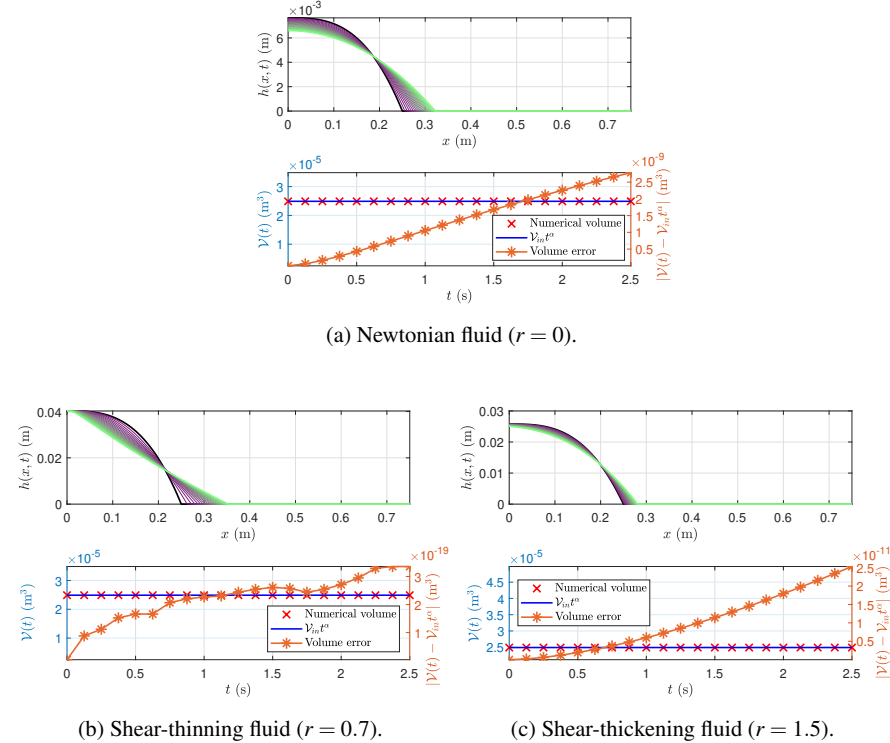


Fig. 6 Results of the conservation study for the release of a fixed fluid mass. To highlight the scheme’s capabilities, each case features a different HS cell: (a) $n = 0$, (b) $n = 0.7$, and (c) $n = 0.5$. The currents are allowed to propagate from $t_0 = 0$ s up to $t_f = 2.5$ s, through 2500 time steps ($\Rightarrow \Delta t = 10^{-3}$ s). In all cases, $\alpha = 0$ and $V_{in} = 2.4902 \times 10^{-5}$ m³. The remaining model parameters for these simulations are the same as in figure 3.

5 Conclusions and Outlook

In this chapter, we developed and benchmarked a finite-difference numerical scheme for solving a family of nonlinear parabolic PDEs with variable coefficients given by eq. (1). A special feature of these nonlinear PDEs is that they possess solutions that can propagate in a wave-like manner with a finite speed of propagation. Our featured example from this family of PDEs was the one-dimensional spreading (propagation) of a power-law (Oswald–de Weale) fluid in a horizontal, narrow fracture with variable width. We placed an emphasis on designing a series of numerical tests that show conclusively that the proposed scheme is second-order accurate in space and time. Analytical self-similar solutions for special cases of the nonlinear parabolic PDE considered were used to benchmark the numerical method. Furthermore, we verified that a global mass conservation/injection constraint can be successfully re-

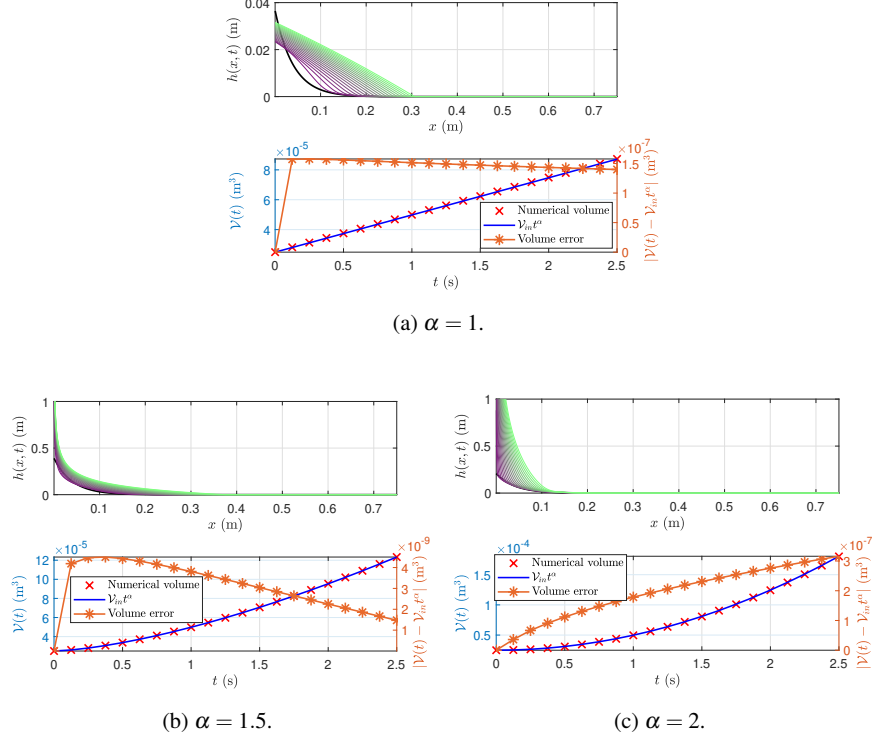


Fig. 7 Results of the conservation study for mass injection. The volume exponent α is varied through three separate cases. We simulate (a) a Newtonian fluid in uniform HS cell ($r = 1, n = 0$), (b) a shear-thinning fluid in a variable width HS cell ($r = 0.7, n = 0.7$), and (c) a shear-thickening fluid in a variable width HS cell ($r = 1.5, n = 0.5$). In all cases, $\mathcal{V}_{in}, t_0, t_f, \Delta t$ are as in figure 6. The remaining model parameters for these simulations are the same as in figure 3.

formulated into a set of nonlinear boundary conditions, which were implemented with second-order accuracy as well.

The main advantage of the finite-difference scheme discussed above is that it is strongly implicit, generalizing the time-stepping suggested by Crank and Nicolson [54]. Therefore, the proposed scheme does not formally require a time-step restriction for stability. By using a staggered grid, along the lines of Christov and Homsy [56], nonlinear terms can be handled within the same three-point stencil as the classical Crank–Nicolson scheme. This choice of grid is particularly convenient for the discretization of the nonlinear boundary conditions, allowing second-order accuracy to be achieved with just a two-point stencil near the domain boundaries. Using fractional steps in time (‘internal iterations’), we reformulated the nonlinear algebraic problem at each time step as a fixed-point iteration.

In future work, an interesting extension to our proposed numerical scheme could be the inclusion of a generic source term of the form $\mathcal{S}(x, t, h)$, added to the right-

hand side of eq. (1). Such a term can capture the effects of e.g., a leaky (porous) substrate over which a gravity current propagates, in which case $\mathcal{S}(x, t, h) = -\kappa h(x, t)$ for some drainage constant κ [65] (see also [25, §9.2]). Then, the Crank–Nicolson discretization in eq. (11) could be modified by adding

$$\frac{1}{2} [\mathcal{S}(x_i, t^{n+1}, h_i^{n+1}) + \mathcal{S}(x_i, t^n, h_i^n)] \quad (28)$$

to the right-hand side. Here, it is assumed that $\partial h / \partial x$ does not appear in \mathcal{S} but only in \mathcal{L} . Therefore, the discretization in eq. (28) (even if nonlinear) will, at most, introduce a term in the matrix diagonal coefficient and a term on the right-hand side of eq. (18). Another variation on this theme involves the spreading of an unconfined viscous fluid above a deep porous medium into which it penetrates in a time-dependent manner over a depth of $l(x, t)$ [53]. Then, $\mathcal{S}(x, t, h) = -\kappa[1 + h(x, t)/l(x, t)]$ and an additional ODE for $l(x, t)$ is coupled to eq. (1). This problem is an interesting avenue for future extension of our proposed scheme, as we would have to discretize the ODE for $l(x, t)$ in the same Crank–Nicolson sense as eq. (1) and add an extra equation (row) to the discrete problem in eq. (18).

On the other hand, an inclination angle (recall that all geometries in figure 1 are lying flat, so gravity is directed in the $-y$ -direction) results in a term proportional to $\partial h / \partial x$ being added to eq. (1) (for the case of a Newtonian fluid, see, e.g., [29, 32]). This additional term changes the nonlinear diffusion equation (1) into a nonlinear *advection–diffusion* equation. Care must be taken in discretizing this new advective term. A similar PDE arises in the segregation of bidisperse granular mixtures [66, 67]. As discussed by Christov [68], a strongly implicit Crank–Nicolson scheme can be successfully used for these problems. The scheme in [68] is so robust that it performs well even in the singular vanishing-diffusivity limit of the advection-diffusion equation. Considering a generic advection term $\partial \Psi(h) / \partial x$, it can be handled analogously to the nonlinearity in the diffusion term. Specifically, we approximate

$$\left(\frac{\partial \Psi}{\partial x} \right)_{x=x_i} \approx \frac{1}{2} \left[\left(\frac{\Psi_{i+1}^{n+1} - \Psi_{i-1}^{n+1}}{2\Delta x} \right) + \left(\frac{\Psi_{i+1}^n - \Psi_{i-1}^n}{2\Delta x} \right) \right]. \quad (29)$$

Here, the advective term is discretized through a central difference formula involving a local three-point stencil on all interior nodes ($i = 1$ to $N - 1$). At the boundary nodes ($i = 0$ and $i = N$), one can use a three-point biased (forward or backward) difference formula, as described in eqs. (17). The now well-established idea of staggering the nonlinear term across fractional time steps is carried forward (recall eqs. (15)). However, to properly linearize the advective term within the internal iterations, we must be able to write $\Psi(h) = \Upsilon(h)h$ (the most obvious way being $\Upsilon(h) \equiv \Psi(h)/h$) so that

$$\Psi_{i\pm 1}^{n+1} \approx \Upsilon_{i\pm 1}^{n+1/2,k} h_{i\pm 1}^{n+1,k}. \quad (30)$$

Then, inserting eq. (30) into eq. (29) and adding the result to the left-hand side of eq. (18), modifies the tridiagonal system by adding $\Upsilon_{i\pm 1}^{n+1/2,k} / (4\Delta x)$ to the superdiag-

onal ($i + 1$) and subdiagonal ($i - 1$). The remaining terms from eq. (29) are added to the right-hand side of the system.

Any of these potential extensions would have to be benchmarked against available first-kind self-similar solutions in [25, 29, 32, 53], however, no particular difficulties are expected to arise.

Another avenue of future work is as follows. Nowadays, high-order (i.e., greater than second-order) nonlinear parabolic PDEs are found to describe a wealth of low Reynolds number fluid phenomena: from the spreading and healing [64, 69] to the rupture dynamics [70] of thin liquid films dominated by capillary forces (see also [21, Ch. 6-C]). Typically, the spatial operator is of fourth order due to the inclusion of surface tension effects (which depend upon the curvature of h), making the PDE more challenging to solve numerically. (Note that this is distinct from the inclusion of capillary effects in the context of gravity currents propagating in porous media described above, see [71].) Even higher (sixth) order thin film equations arise in dynamics of lubricated thin elastic membranes [72, 73] dominated by elastic forces. To interrogate these complex interfacial phenomena, there is a current need for a robust and accurate numerical scheme to simulate these flows with low computational overhead (e.g., without the prohibitive time step stability restrictions of explicit schemes). In future work, it would be of interest to generalize the scheme from this chapter to such problems. Additionally, non-uniform (or adaptive) grids, which could be implemented along the lines of [58], can be used to capture singularity formation during thin film rupture.

Acknowledgements We dedicate this work to the 80th anniversary of Prof. Jüri Engelbrecht and his contributions to the fields of complexity science, nonlinear wave phenomena and applied mathematical modeling. I.C.C. acknowledges a very productive trip to Tallinn in September of 2014 (on invitation of Prof. Andrus Salupere) and fondly recalls meeting and interacting with Prof. Engelbrecht there, at the IUTAM Symposium on Complexity of Nonlinear Waves.

We also thank Profs. Tarmo Soomere and Arkadi Berezovski for their efforts in editing this volume and their kind invitation to contribute a chapter. Finally, I.C.C. acknowledges many helpful conversations on gravity currents with Prof. H.A. Stone, Dr. Z. Zheng and Prof. S. Longo. Specifically, we thank S. Longo for suggesting the form of the governing equation for a power-law fluid in a variable-width HS cell (third row in table 1).

Appendix

For many natural phenomena, a relatively simple procedure involving a scaling (dimensional analysis) of their physical model can be used to yield the similarity variable and appropriate rescaling necessary to obtain a first-kind self-similar solution [24]. Viscous gravity currents exhibit such self-similar propagation, meaning that the solution (at sufficiently ‘long’ times [24]) depends solely upon a combined variable of x and t , rather than on each independently. Self-similarity allows for the derivation of exact analytical solutions to the governing equation (1) against which numerical solutions can be benchmarked. Specifically, for the case of the release of

a fixed mass of fluid ($\alpha = 0$ so that $\mathcal{V}(t) = \mathcal{V}_{\text{in}} \forall t \in [t_0, t_f]$), a closed-form analytical self-similar solution was used in §4.1 to test the order of convergence of the numerical scheme.

In this Appendix, following Di Federico et al [43], we summarize the derivation of said self-similar solution for a power-law non-Newtonian fluid spreading *away* from the origin ($x = 0$) of a HS cell of uniform width b_1 ($n = 0$).³ First, we introduce the following dimensionless variables (with $*$ superscripts) from [43]:

$$x^* = \left(\frac{B}{A^\alpha} \right)^{1/(\alpha-2)} x, \quad t^* = \left(\frac{B}{A^2} \right)^{1/(\alpha-2)} t, \\ h^*(x^*, t^*) = \left(\frac{B}{A^\alpha} \right)^{1/(\alpha-2)} h(x, t), \quad (31)$$

where A is the constant from eq. (1) (defined in table 1) and $B = \mathcal{V}_{\text{in}}/b_1$. Hereafter, we drop the $*$ superscripts. Next, we must select a suitable similarity variable η . As discussed in §1, a self-similar solution of the first kind has the form $h(x, t) = t^\beta f(\eta)$ with $\eta = x/t^\delta$. Then, a scaling analysis of dimensionless version of eq. (1) yields

$$h(x, t) = \eta_N^{r+1} t^{F_2} f(\zeta), \quad \eta = \frac{x}{t^{F_1}}, \quad \zeta = \frac{\eta}{\eta_N}. \quad (32)$$

It can be shown that the constant η_N specifically corresponds to the value of η at the nose of the current, i.e., $\eta_N = x_f(t)/t^{F_1}$, where $x = x_f(t)$ is such that $h(x_f(t), t) = 0$. Here, ζ is a convenient rescaled similarity variable, and the exponents $F_{1,2}$ are

$$F_1 = \frac{\alpha + r}{r + 2}, \quad (33a)$$

$$F_2 = \alpha - F_1. \quad (33b)$$

The shape function $f(\zeta)$ represents the (universal) self-similar profile of the gravity current. We must now determine this function, by substituting eqs. (32) into the dimensionless version of eq. (1) to reduce the latter to a nonlinear ODE:

$$\frac{d}{d\zeta} \left(f \left| \frac{df}{d\zeta} \right|^{\frac{1}{r}} \right) + F_2 f - F_1 \zeta \frac{df}{d\zeta} = 0, \quad \zeta \in [0, 1]. \quad (34)$$

The second-order ODE in eq. (34) can be rewritten as a first-order system:

$$\frac{d}{d\zeta} \begin{Bmatrix} f_1 \\ f_2 \end{Bmatrix} = \begin{Bmatrix} -r \\ f_2 \end{Bmatrix} \left[f_2 |f_2|^{(1-2r)/r} + F_2 f_1 - F_1 \zeta f_2 \right], \quad (35)$$

³ While self-similar reductions are, of course, also possible for $n > 0$, they do not yield closed-form analytical solutions.

where, for convenience, we have set $f_1 = f$. The system in eq. (35) is ‘stiff,’ and we must use an appropriate ODE solver, such as `ode15s` in MATLAB, subject appropriate initial and/or boundary conditions at $\zeta = 0, 1$.

A peculiarity of this self-similar analysis is that we have only a single BC for the ODE (34), namely $f(1) = 0$, i.e., this is the location of the gravity current’s nose $x = x_f(t)$ at which $\zeta = \eta/\eta_N = 1$ and $h(x_f(t), t) = 0$. Since the ODE in eq. (35) requires a second initial or boundary condition, we use the ‘backwards-shooting’ idea introduced by Huppert [20] to provide a second condition near $\zeta = 1$. Then, the ODE in eq. (35) can be integrated ‘backwards’ from $\zeta = 1$ to $\zeta = 0$ subject to two ‘initial’ conditions at $\zeta = 1$.

To this end, consider the asymptotic behavior of the current near the nose. By assuming that $f \sim c_1(1 - \zeta)^{c_2}$ as $\zeta \rightarrow 1^-$ and substituting this expression into eq. (34), we obtain $c_1 = F_2^r$ and $c_2 = 1$ by balancing the lowest-order terms. Now, we have two BCs (see also [43]):

$$f_1(1 - \varepsilon) = F_2^r \varepsilon, \quad (36a)$$

$$f_2(1 - \varepsilon) = -F_2^r, \quad (36b)$$

for a sufficiently small $\varepsilon \ll 1$. We can now solve the system (35) subject to the ‘final’ conditions (36) on the interval $\zeta \in [0, 1 - \varepsilon]$. By convention, an ODE is solved with initial, not final, conditions. Therefore, we perform the transformation $\zeta \mapsto 1 - \hat{\zeta}$, which leads to the right-hand-side of eq. (35) being multiplied by -1 . Then, the final conditions in eqs. (36) become initial conditions at $\hat{\zeta} = \varepsilon$, and the first-order system of ODEs is solved on the interval $\hat{\zeta} \in [\varepsilon, 1]$.

For certain special cases, a closed-form analytical solution to eq. (34) can be obtained. For the case of the release of a fixed mass of fluid ($\alpha = 0$), Ciriello et al [44] derived such an exact solution (can be verified by substitution):

$$f(\zeta) = \frac{r^r}{(r+2)^r(r+1)} (1 - \zeta^{r+1}), \quad (37)$$

which we used to benchmark our finite-difference scheme in §4.1. Finally, to obtain the viscous gravity current profile given in eq. (32) we must compute η_N . This value follows from imposing the mass conservation constraint in dimensionless form:

$$\eta_N = \left[\int_0^1 f(\zeta) d\zeta \right]^{-1/(r+2)} \approx \left[\int_\varepsilon^1 f(\hat{\zeta}) d\hat{\zeta} \right]^{-1/(r+2)}, \quad (38)$$

where the second (approximate) equality is needed for the case in which eq. (34) has to be integrated numerically (no exact solution); $\varepsilon \ll 1$ is chosen sufficiently small, as above.

Finally we can combine eqs. (37) and (38) into eq. (32), and analytically obtain the height profile over the fluid domain x at some time t . It should be noted, however, that for this solution to apply, the current must be in its self-similar regime, having forgotten any arbitrary initial condition from which it has evolved.

References

- [1] Engelbrecht J (2015) Questions About Elastic Waves. Springer International Publishing, Cham, Switzerland, DOI 10.1007/978-3-319-14791-8
- [2] Christov IC (2014) Wave solutions. In: Hetnarski RB (ed) Encyclopedia of Thermal Stresses, Springer, Netherlands, pp 6495–6506, DOI 10.1007/978-94-007-2739-7_33
- [3] Kolmogorov A, Petrovskii I, Piskunov N (1991) A study of the diffusion equation with increase in the amount of substance, and its application to a biological problem. In: Tikhomirov VM (ed) Selected Works of A. N. Kolmogorov, Mathematics and Its Applications (Soviet Series), vol 25, Springer, Dordrecht, pp 248–270, DOI 10.1007/978-94-011-3030-1_38, translation of 1937 Russian original
- [4] Fisher RA (1937) The wave of advance of advantageous genes. *Ann Eugenics* 7:353–369, DOI 10.1111/j.1469-1809.1937.tb02153.x
- [5] Barenblatt GI (1952) On some unsteady fluid and gas motions in a porous medium (in Russian). *Prikl Mat Mekh (PMM)* 16:67–78
- [6] Ostriker JP, Barenblatt GI, Sunyaev RA (eds) (1992) Selected Works of Yakov Borisovich Zeldovich, vol 1. Princeton University Press, Princeton, NJ
- [7] Engelbrecht J (1997) Nonlinear Wave Dynamics: Complexity and Simplicity, Kluwer Texts in the Mathematical Sciences, vol 17. Springer Science+Business Media, Dordrecht, DOI 10.1007/978-94-015-8891-1
- [8] Vlasov SN, Talanov VI (1995) The parabolic equation in the theory of wave propagation. *Radiophys Quantum Electron* 38:1–12, DOI 10.1007/BF01051853
- [9] Jerzak W, Collins MD, Evans RB, Lingevitch JF, Siegmann WL (2002) Parabolic equation techniques for seismic waves. *Pure Appl Geophys* 159:1681–1689, DOI 10.1007/s00024-002-8702-2
- [10] Jensen FB, Kuperman WA, Porter MB, Schimdt H (2011) Computational Ocean Acoustics, 2nd edn. Springer Science+Business Media, New York, DOI 10.1007/978-1-4419-8678-8
- [11] Engelbrecht J, Peets T, Tamm K, Laasmaa M, Vendelin M (2018) On the complexity of signal propagation in nerve fibres. *Proc Estonian Acad Sci* 67:28–38, DOI 10.3176/proc.2017.4.28
- [12] Engelbrecht J, Salupere A, Berezovski A, Peets T, Tamm K (2018) On nonlinear waves in media with complex properties. In: Altenbach H, Pouget J, Rousseau M, Collet B, Michelitsch T (eds) Generalized Models and Non-classical Approaches in Complex Materials 1, Advanced Structured Materials, vol 89, Springer International Publishing, Cham, Switzerland, pp 248–270, DOI 10.1007/978-3-319-72440-9_13
- [13] Christov CI, Maugin GA, Porubov AV (2007) On Boussinesq's paradigm in nonlinear wave propagation. *C R Mecanique* 335:521–535, DOI 10.1016/j.crme.2007.08.006
- [14] Evans LC (2010) Partial Differential Equations, Graduate Studies in Mathematics, vol 19, 2nd edn. American Mathematical Society, Providence, RI
- [15] Zel'dovich YB, Raizer YP (2002) Physics of Shock Waves and High-Temperature Hydrodynamic Phenomena. Dover Publications, Mineola, NY, edited by W. D. Hayes and R. F. Probstein
- [16] Straughan B (2011) Heat Waves, Applied Mathematical Sciences, vol 117. Springer Science+Business Media, New York, NY, DOI 10.1007/978-1-4614-0493-4
- [17] Berezovski A, Ván P (2017) Internal Variables in Thermoelasticity, Solid Mechanics and Its Applications, vol 243. Springer International Publishing, Cham, Switzerland, DOI 10.1007/978-3-319-56934-5
- [18] Gilding BH, Kersner R (2004) Travelling Waves in Nonlinear Diffusion-Convection Reaction, Progress in Nonlinear Differential Equations and Their Applications, vol 60. Birkhäuser Verlag, Basel, Switzerland, DOI 10.1007/978-3-0348-7964-4
- [19] Vázquez JL (2007) The Porous Medium Equation: Mathematical Theory. Oxford University Press, Oxford, UK, DOI 10.1093/acprof:oso/9780198569039.001.0001

- [20] Huppert HE (1982) The propagation of two-dimensional and axisymmetric viscous gravity currents over a rigid horizontal surface. *J Fluid Mech* 121:43–58, DOI 10.1017/S0022112082001797
- [21] Leal LG (2007) Advanced Transport Phenomena: Fluid Mechanics and Convective Transport Processes. Cambridge University Press, New York, DOI 10.2277/0521849101
- [22] Didden N, Maxworthy T (1982) Viscous spreading of plane and axisymmetric gravity waves. *J Fluid Mech* 121:27–42, DOI 10.1017/S0022112082001785
- [23] Barenblatt GI, Zel'dovich YB (1972) Self-similar solutions as intermediate asymptotics. *Annu Rev Fluid Mech* 4:285–312, DOI 10.1146/annurev.fl.04.010172.001441
- [24] Barenblatt GI (1996) Similarity, Self-Similarity, and Intermediate Asymptotics, Cambridge Texts in Applied Mathematics, vol 14. Cambridge University Press, DOI 10.1017/CBO9781107050242
- [25] Woods AW (2015) Flow in Porous Rocks: Energy and Environmental Applications. Cambridge University Press, Cambridge, UK, DOI 10.1017/CBO9781107588677
- [26] Bear J (1988) Dynamics of Fluids in Porous Media. Dover Publications, Mineola, NY
- [27] Huppert HE (2000) Geological fluid mechanics. In: Batchelor GK, Moffatt HK, Worster MG (eds) Perspectives in Fluid Dynamics, Cambridge University Press, pp 447–506
- [28] Huppert HE, Neufeld JA (2014) The fluid mechanics of carbon dioxide sequestration. *Annu Rev Fluid Mech* 46:255–272, DOI 10.1146/annurev-fluid-011212-140627
- [29] Huppert HE, Woods AW (1995) Gravity driven flows in porous layers. *J Fluid Mech* 292:55–69, DOI 10.1017/S0022112095001431
- [30] Anderson DM, McLaughlin RM, Miller CT (2003) The averaging of gravity currents in porous media. *Phys Fluids* 15:2810–2829, DOI 10.1063/1.1600733
- [31] Lyle S, Huppert HE, Hallworth M, Bickle M, Chadwick A (2005) Axisymmetric gravity currents in a porous medium. *J Fluid Mech* 543:293–302, DOI 10.1017/S0022112005006713
- [32] Vella D, Huppert HE (2006) Gravity currents in a porous medium at an inclined plane. *J Fluid Mech* 555:353–362, DOI 10.1017/S0022112006009578
- [33] Hesse MA, Tchelepi HA, Cantwell BJ, Orr Jr FM (2007) Gravity currents in horizontal porous layers: transition from early to late self-similarity. *J Fluid Mech* 577:363–383, DOI 10.1017/S0022112007004685
- [34] Anderson DM, McLaughlin RM, Miller CT (2010) A sharp-interface interpretation of a continuous density model for homogenization of gravity-driven flow in porous media. *Phys D* 239:1855–1866, DOI 10.1016/j.physd.2010.06.009
- [35] De Loubens R, Ramakrishnan TS (2011) Analysis and computation of gravity-induced migration in porous media. *J Fluid Mech* 675:60–86, DOI 10.1017/S0022112010006440
- [36] Ciriello V, Di Federico V, Archetti R, Longo S (2013) Effect of variable permeability on the propagation of thin gravity currents in porous media. *Int J Non-linear Mech* 57:168–175, DOI 10.1016/j.ijnonlinmec.2013.07.003
- [37] Huppert HE, Neufeld JA, Strandkvist C (2013) The competition between gravity and flow focusing in two-layered porous media. *J Fluid Mech* 720:5–14, DOI 10.1017/jfm.2012.623
- [38] Zheng Z, Christov IC, Stone HA (2014) Influence of heterogeneity on second-kind self-similar solutions for viscous gravity currents. *J Fluid Mech* 747:218–246, DOI 10.1017/jfm.2014.148
- [39] Gratton J, Mahajan SM, Minotti F (1999) Theory of creeping gravity currents of a non-Newtonian liquid. *Phys Rev E* 60:6090–6097, DOI 10.1103/PhysRevE.60.6960
- [40] Perazzo CA, Gratton J (2003) Thin film of non-Newtonian fluid on an incline. *Phys Rev E* 67:016307, DOI 10.1103/PhysRevE.67.016307
- [41] Perazzo CA, Gratton J (2005) Exact solutions for two-dimensional steady flows of a power-law liquid on an incline. *Phys Fluids A* 17:013102, DOI 10.1063/1.1829625
- [42] Di Federico V, Archetti R, Longo S (2012) Similarity solutions for spreading of a two-dimensional non-Newtonian gravity current in a porous layer. *J Non-Newtonian Fluid Mech* 177–178:46–53, DOI 10.1016/j.jnnfm.2012.04.003

- [43] Di Federico V, Longo S, King SE, Chiapponi L, Petrolo D, Ciriello V (2017) Gravity-driven flow of Herschel–Bulkley fluid in a fracture and in a 2D porous medium. *J Fluid Mech* 821:59–84, DOI 10.1017/jfm.2017.234
- [44] Ciriello V, Longo S, Chiapponi L, Federico D (2016) Porous gravity currents: A survey to determine the joint influence of fluid rheology and variations of medium properties. *Adv Water Res* 92:105–115, DOI 10.1016/j.advwatres.2016.03.021
- [45] Gratton J, Minotti F (1990) Self-similar viscous gravity currents: phase plane formalism. *J Fluid Mech* 210:155–182, DOI 10.1017/S0022112090001240
- [46] Gratton J (1991) Similarity and self similarity in fluid dynamics. *Fund Cosmic Phys* 15:1–106
- [47] Diez JA, Gratton R, Gratton J (1992) Self-similar solution of the second kind for a convergent viscous gravity current. *Phys Fluids A* 6:1148–1155, DOI 10.1063/1.858233
- [48] Alhashim MG, Koch DL (2018) The effects of fluid transport on the creation of a dense cluster of activated fractures in a porous medium. *J Fluid Mech* 847:286–328, DOI 10.1017/jfm.2018.313
- [49] Bird RB, Armstrong RC, Hassager O (1987) Dynamics of Polymeric Liquids, vol 1, 2nd edn. John Wiley, New York
- [50] Oron A, Davis SH, Bankoff SG (1997) Long-scale evolution of thin liquid films. *Rev Mod Phys* 69:931–980, DOI 10.1103/RevModPhys.69.931
- [51] Boyko E, Bercovici M, Gat AD (2017) Viscous-elastic dynamics of power-law fluids within an elastic cylinder. *Phys Rev Fluids* 2:073301, DOI 10.1103/PhysRevFluids.2.073301
- [52] Bonnecaze RT, Huppert HE, Lister JR (1993) Particle-driven gravity currents. *J Fluid Mech* 250:339–369, DOI 10.1017/S002211209300148X
- [53] Acton JM, Huppert HE, Worster MG (2001) Two-dimensional viscous gravity currents flowing over a deep porous medium. *J Fluid Mech* 440:359–380, DOI 10.1017/S002211200100516X
- [54] Crank J, Nicolson P (1947) A practical method for numerical evaluation of solutions of partial differential equations of the heat-conduction type. *Math Proc Camb Phil Soc* 43:50–67, DOI 10.1017/S0305004100023197
- [55] Strikwerda J (2004) Finite Difference Schemes and Partial Differential Equations, 2nd edn. Society for Industrial and Applied Mathematics, DOI 10.1137/1.9780898717938
- [56] Christov CI, Homsy GM (2009) Enhancement of transport from drops by steady and modulated electric fields. *Phys Fluids* 21:083102, DOI 10.1063/1.3179555
- [57] Yanenko NN (1971) The Method of Fractional Steps. Springer-Verlag, Berlin/Heidelberg, DOI 10.1007/978-3-642-65108-3, english translation edited by M. Hoult
- [58] Christov CI, Deng K (2002) Numerical investigation of quenching for a nonlinear diffusion equation with a singular Neumann boundary condition. *Numer Methods Partial Differential Eq* 18:429–440, DOI 10.1002/num.10013
- [59] Von Rosenberg DU (1975) Methods for the Numerical Solution of Partial Differential Equations, Modern Analytic and Computational Methods in Science and Mathematics, vol 16, 3rd edn. Elsevier, New York
- [60] Douglas Jr J, Peaceman DW, Rachford Jr HH (1959) A method for calculating multidimensional immiscible displacement. *Petrol Trans, AIME* 216:297–308, URL <https://www.onepetro.org/general/SPE-1327-G>
- [61] Douglas Jr J, Peaceman DW, Rachford Jr HH (1962) Numerical calculation of multidimensional miscible displacement. *Soc Petrol Eng J* 2:327–339, DOI 10.2118/471-PA
- [62] Cheng NS (2008) Formula for the viscosity of a glycerol-water mixture. *Ind Eng Chem Res* 47:3285–3288, DOI 10.1021/ie071349z
- [63] Volk A, Kähler C (2018) Density model for aqueous glycerol solutions. *Exp Fluids* 59:75, DOI 10.1007/s00348-018-2527-y
- [64] Zheng Z, Fontelos M, Shin S, Stone HA (2018) Universality in the nonlinear leveling of capillary films. *Phys Rev Fluids* 3:032001, DOI 10.1103/PhysRevFluids.3.032001
- [65] Pritchard D, Woods AW, Hogg AJ (2001) On the slow draining of a gravity current moving through a layered permeable medium. *J Fluid Mech* 444:23–47, DOI 10.1017/S002211200100516X

- [66] Dolgunin VN, Ukolov AA (1995) Segregation modeling of particle rapid gravity flow. Powder Technol 83:95–103, DOI 10.1016/0032-5910(94)02954-M
- [67] Gray JMNT, Gajjar P, Kokelaar P (2015) Particle-size segregation in dense granular avalanches. C R Phys 16:73–85, DOI 10.1016/j.crhy.2015.01.004
- [68] Christov IC (2018) On the numerical solution of a variable-coefficient Burgers equation arising in granular segregation. Mat Phys Mech 35:21–27, DOI 10.18720/MPM.3512018_4
- [69] Zheng Z, Fontelos M, Shin S, Michael MD, Tseluiko D, Kalliadasis S, Stone HA (2018) Healing capillary films. J Fluid Mech 838:404–434, DOI 10.1017/jfm.2017.777
- [70] Garg V, Kamat PM, Anthony CR, Thete SS, Basaran OA (2017) Self-similar rupture of thin films of power-law fluids on a substrate. J Fluid Mech 826:455–483, DOI 10.1017/jfm.2017.446
- [71] Golding MJ, Neufeld JA, Hesse MA, Huppert HE (2011) Two-phase gravity currents in porous media. J Fluid Mech 678:248–270, DOI 10.1017/jfm.2011.110
- [72] Hosoi AE, Mahadevan L (2004) Peeling, healing, and bursting in a lubricated elastic sheet. Phys Rev Lett 93:137802, DOI 10.1103/PhysRevLett.93.137802
- [73] Flitton JC, King JR (2004) Moving-boundary and fixed-domain problems for a sixth-order thin-film equation. Eur J Appl Math 15:713–754, DOI 10.1017/S0956792504005753